JGR Solid Earth

RESEARCH ARTICLE
10.1029/2025JB031780

Continent-Side Paleo-Rift Structure in the Western East Sea (Sea of Japan) and Linkage Between Moho Uplift and Mountain Range Formation

Jeongin Lee[1], Tae-Kyung Hong[1], Junhyung Lee[1], Seongjun Park[1], Byeongwoo Kim[1], Samuel Celis[1], and Yanbing Liu[1]

[1]Department of Earth System Sciences, Yonsei University, Seoul, South Korea

Key Points:

- The crustal structure in the east-central Korean Peninsula reveals the continent-side paleo-rift geometry
- An uplifted Moho and high seismic velocity anomalies along the coast suggest rift-flank structures
- The continental rift led to the Taebaek Mountain Range development on the rift flank with Moho uplift near the rift center

Supporting Information:

Supporting Information may be found in the online version of this article.

Correspondence to:

T.-K. Hong,
tkhong@yonsei.ac.kr

Citation:

Lee, J., Hong, T.-K., Lee, J., Park, S., Kim, B., Celis, S., & Liu, Y. (2025). Continent-side paleo-rift structure in the western East Sea (Sea of Japan) and linkage between Moho uplift and mountain range formation. *Journal of Geophysical Research: Solid Earth*, *130*, e2025JB031780. https://doi.org/10.1029/2025JB031780

Received 12 APR 2025
Accepted 19 SEP 2025

Author Contributions:

Conceptualization: Tae-Kyung Hong
Data curation: Junhyung Lee, Seongjun Park, Byeongwoo Kim
Formal analysis: Jeongin Lee
Funding acquisition: Tae-Kyung Hong
Investigation: Jeongin Lee, Tae-Kyung Hong, Junhyung Lee, Byeongwoo Kim, Samuel Celis, Yanbing Liu
Methodology: Jeongin Lee, Tae-Kyung Hong
Resources: Junhyung Lee, Seongjun Park, Byeongwoo Kim
Supervision: Tae-Kyung Hong
Validation: Jeongin Lee

Abstract The continental-side paleo-rift structure in the east-central Korean Peninsula is investigated using joint inversion of receiver functions and surface-wave dispersions based on dense seismic networks. The joint inversion analysis provides precise constraints on crustal thickness and V_P/V_S ratios, and high-resolution 3-D shear-wave velocity model. The model reveals distinct lateral and vertical variations associated with tectonic evolution during continental rifting. Inland regions exhibit typical continental crustal thickness (~33 km) and moderate V_P/V_S ratios (1.60–1.75). On the other hand, coastal regions present shallower Moho depths (~24 km), high V_P/V_S ratios (1.8–1.9), and laterally deformed crustal structures to reflect continental-to-oceanic transition. Low-velocity anomalies at shallow depths (≤3 km) and strong velocity contrasts in the middle and lower crust correlate with sedimentary basins and major faults, indicating tectonic boundaries that influence regional seismicity. Coastal high-velocity anomalies at depth (~30 km) suggest localized mantle uplift related to rifting. Moho uplift near the coast, together with the asymmetric uplift of the Taebaek Mountain Range, indicates depth-dependent lithospheric stretching and isostatic rebound during rifting. These observations are consistent with geological evidence of East Sea (Sea of Japan) opening, highlighting the offshore rift center and its influence on onshore crustal structure. The results provide new constraints on rift-related processes, including lithospheric thinning, mantle upwelling, and asymmetric rift-flank uplift, demonstrating the role of paleo-rift structures in controlling present-day seismicity.

Plain Language Summary The continental rifting in the East Sea (Sea of Japan) separated the Japanese islands from the Korean Peninsula. The rifting history is imprinted in the crustal structures and surface morphology. To better understand the continent-side paleo-rift structure, we investigate a three-dimensional shear-wave velocity model using a joint inversion method combining receiver function analysis and surface-wave dispersion based on dense seismic networks. We resolve the vertical and lateral variations in crustal structures. The results present that the inland crust is thick (~33 km), while the coastal crust is thinner (~24 km). The thin crust near the coast suggests Moho uplift near the rift center. The Taebaek Mountain Range, which rises along the east coast, is linked to the thinning and stretching of the crust. The mountain range parallel to the coastline and uplifted Moho suggest the lithospheric deformation during continental rifting. This paleo-rifting affects the present-day geology and earthquakes.

1. Introduction

Crustal structures around continental rift provide key evidences for reconstruction of tectonic evolutions in continental margin such as lithospheric extension, crustal thinning, Moho uplift, and mantle upwelling. Moreover, paleo-rift zones are mechanically weak, being often reactivated seismically (Choi et al., 2012). Thus, the paleo-rift structures receive attention due to their seismic hazard potentials (Hong et al., 2024).

The continental rifting incorporates surface-topography changes as well as crustal deformation (Bahat & Paul, 1987; Brown & Phillips, 1999; Chèry et al., 1992; Sachau et al., 2013; Weissel & Karner, 1989). The rift flank and Moho are uplifted by isostatic rebounding (flexural uplift) or mantle upwelling (thermal uplift) during the rifting (Bahat & Paul, 1987; Braun & Beaumont, 1989; Chèry et al., 1992; Sachau & Koehn, 2010; Weissel & Karner, 1989). Lithospheric rigidity controls the flank uplift (Chèry et al., 1992; Sachau et al., 2013; Sachau & Koehn, 2010). Thus, surface topography and Moho depth variation may enable us to constrain the rift structures. Also, high-resolution crustal structure may present the clues for the crustal configuration and surface topography at present.

Visualization: Jeongin Lee
Writing – original draft: Jeongin Lee, Tae-Kyung Hong
Writing – review & editing: Tae-Kyung Hong

The continental rifting in the eastern margin of Eurasian Plate in late Oligocene (~27–23 Ma) to mid-Miocene (~23–15 Ma) separate the Japanese islands from the Korean Peninsula, forming the East Sea (Sea of Japan) (Choi et al., 2012; Jolivet et al., 1994; Otofuji, 1996). The associated tectonic processes from rifting to seafloor spreading formed various rift-axis parallel structures along the east coast of the Korean Peninsula (Kim et al., 2007, 2015, 2022). The continental rifting decreased gradually with time, and ceased in late Miocene (~15–12 Ma) under the dominant compressional stress field (Choi et al., 2012; Itoh et al., 2006; Yoon & Chough, 1995).

The eastern Korean Peninsula was influenced by the consistent uplift during the late Quaternary (~200 ka) (Kim et al., 2016). The continental-rift structures have been modified by subsequent deformation processes including tectonic reactivation in late Pleistocene (~125 ka), causing long-term isostatic response to the earlier extensional deformation (Kim et al., 2016). A 500-km-long coastline-parallel structure, Taebaek Mountain Range (TBR) receives considerable attention due to its linkage with the continental rift. The TBR was uplifted rapidly in the period of East Sea opening (~22 Ma) (Cho et al., 2018). However, the details of such high mountain formation along the coast remain poorly understood. Also, there are gaps in understanding between the continental rift and current crustal configuration (Choi et al., 2012; Cukur et al., 2018; Kim et al., 2015, 2023).

Seismic tomography studies are useful to explore the lithospheric structures. They help us to understand the tectonic process linked to the continental rift (Hong & Kang, 2009; Shin & Sandiford, 2012). Recently, a seismic tomography study identified the continental-rift signatures such as uplifted mantle, solidified underplated magma and anomalous low velocities in upper mantle around the east coast of the Korean Peninsula (Park & Hong, 2024). However, seismic tomographic analyses naturally suffer from limited vertical resolution, leaving uncertainty in vertical extent and interface depth (Rawlinson et al., 2010).

On the other hand, receiver-function analyses based on dense seismic stations may be useful to identify laterally-varying crustal structures. However, previous receiver-function studies in the Korean Peninsula were based on relatively sparse seismic networks, presenting limited resolution on the lateral variation in crustal structures (e.g., Chang & Baag, 2007). We conduct a joint inversion based on receiver functions and surface-wave dispersion to investigate the continent-side crustal structures along the east coast of the Korean Peninsula. The surface wave dispersion constrains the regional velocity structures, while the receiver function determines the seismic discontinuities in the medium. A joint inversion analysis based on dense seismic stations yields fine-scale shear-wave velocity models.

We study the linkage between deep structures (Moho morphology) and surface topography around the continent-side rift flank from the crustal and geological structures, complementing to the large-scale lithospheric structures (Park & Hong, 2024). We interpret the illuminated crustal structures in the context of rift-flank uplift, which suggests the lithospheric response to continental rifting. The uplifted and detached crustal structure may provide information on the continental-rifting episodes and associated crustal deformation (Kim et al., 2007, 2022; Moon et al., 2023).

2. Geology and Geophysical Properties

The East Sea (Sea of Japan) corresponds to a backarc region of the Japanese islands (Chough & Barg, 1987; Tamaki, 1988). It was proposed that the East Sea was opened in response to a continental rifting that started in the Oligocene and ended in the mid-Miocene (Jolivet et al., 1994; Otofuji, 1996). This continental rifting was ceased in the late mid-Miocene due to a stress reversal from an extensional to a compressional regime (Choi et al., 2012; Itoh et al., 2006).

The East Sea opening followed three stages that include (a) back-arc rifting and breakup at the northern margin, (b) back-arc rifting and breakup at the southern margin, and (c) clockwise rotation of the SW Japan Arc away from the Korean Peninsula, which was followed by a back-arc spreading (Kim et al., 2018, 2022). Consequently, the crust of the East Sea has a transitional structure, combining features of continental and oceanic crusts with deep-sea backarc basins (e.g., Japan, Yamato, and Ulleung (Tsushima) basins) and highlands (Korea Plateau, Oki Bank, and Yamato Bank) (Hong, 2010; Hong et al., 2008; Kim et al., 2003; Sato et al., 2006).

The East Sea opening formed complex environment in the continental margin. This tectonic evolution significantly influenced the shaping of the continental margin and the formation of rift-related structures. The central-eastern margin of the Korean Peninsula is extended to a continental fragment (Korea Plateau) in the East Sea (Kim et al., 2007, 2015). A narrow (15–20 km wide) rift basin (Hupo Basin (HB)), an uplifted highland (Hupo bank), and

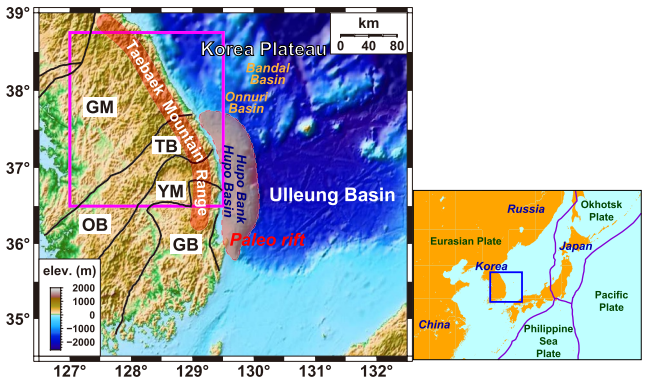

Figure 1. Geological setting around the Korean Peninsula. The study area is marked (boxed area). Major geological provinces and structures are indicated: Gyeonggi massif (GM), Gyeongsang basin (GB), Okcheon belt (OB), Taebaeksan basin (TB), Yeongnam massif (YM), Korean Plateau, Bandal basin, Onnuri basin, and Ulleung basin. Taekbaek mountain range develops along the east coast of the Korean Peninsula. A paleo rift is present off the east coast.

a deep-sea basin (Ulleung Basin (UB)) are located in the offshore region of the southern Korean Peninsula. Earthquakes occur in the paleo-rift structures in the current stress field (Hong et al., 2020). It is noteworthy that the HB is an asymmetrical half-graben that was formed during the first stage of the East Sea opening, while the UB is a deep basin developed by a crustal movement during the final stage (Kim et al., 2022; Yoon & Chough, 1995). The crustal thickness of UB is ∼10 km, which exceeds typical oceanic-crust thicknesses (Kim et al., 2003; Park et al., 2006; Yu, 2006). Most offshore earthquakes in the western East Sea occur in the zone between the east coast and western UB (Hong et al., 2020, 2024).

The Pacific-slab retreat, East Sea opening, and surface uplift in the eastern margin of northeast Asia occurred synchronously during the early Miocene (Shin & Sandiford, 2012). The subduction of the Pacific Plate beneath East Asia formed a stagnant slab in the mantle, which induced hot and wet mantle upwelling, resulting in the Big Mantle Wedge (Zhao, 2021; Zhao et al., 2009). This process, driven by dehydration within the stagnant slab, generated convective upwellings that triggered intraplate volcanism and continental rifting, contributing to the opening of the East Sea (Zhao, 2021; Zhao et al., 2009). The pronounced topographic changes observed along the east coast of Korean Peninsula are likely linked to back-arc rifting during the Oligocene-Miocene period (Cho et al., 2018; Shin & Hwang, 2014).

The east-central Korean Peninsula corresponds to Gangwon Province, a mountain area adjacent to the East Sea (Figure 1). In this region, the Gyeonggi massif and the Okcheon belt (OB) constitute the geological units of the east-central Korean Peninsula (Figure 2). The Gyeonggi massif is a Precambrian shield that is primarily composed of the Gyeonggi gneiss complex, being intruded by granitoids during the Mesozoic (Kim et al., 2006). The OB is a metamorphic fold-thrust belt that was formed in the Triassic (Choi, 2014). The OB can be divided into the southwestern Chungcheong basin and the northeastern Taebaeksan basin (TB) by the South Korean Tectonic Line (Choi, 2014; Kwon et al., 2019).

The Korean Peninsula experienced a series of intense orogenic events and uplifts since the Mesozoic, which led to mountain formation (Choi, 2014). The Daebo orogeny in the Jurassic, attributed to the subduction of the paleo-Pacific plate, gave rise to northeast-southwest tecto-lineaments and folded mountains, including the Charyeong and Gwangju mountain range (Choi, 2014; Park & Son, 2005).

The TBR runs ∼500 km N-S along the east coast, reaching elevations over 1,700 m (Kim et al., 2016). The range shows pronounced topographic asymmetry, with gentle western slopes and steep eastern escarpments facing the East Sea (Sea of Japan). This topographic asymmetry is well-preserved and is interpreted to reflect the Miocene rift-related uplift associated with the back-arc opening of the East Sea during the Oligocene to middle Miocene (Cho et al., 2018; Kim et al., 2016). The range sits on crystalline basement rocks, mainly Mesozoic granites intruding on Precambrian and Paleozoic gneiss and sedimentary units (Cho et al., 2018; Choi, 2014).

Faults running across the study region (e.g., Inje, Keumwang, and Wangsukcheon faults) were produced by tectonic deformation during the Mesozoic (Khulganakhuu et al., 2015; Kil et al., 2021; Park et al., 2023; Zappala et al., 2022). Inje fault (IF) experienced at least three episodes of fault reactivation since the Cretaceous (Khulganakhuu et al., 2015), while Wangsukcheon fault was reactivated in over six distinct episodes during the Quaternary (Bae & Lee, 2016; Chung et al., 2014). Earthquakes are scattered around the fault zones (Hong et al., 2016, 2021; Malehmir et al., 2022; Park et al., 2021).

In addition to structural variations, the Bouguer gravity anomaly, heat flow, and shear-wave velocity at the top 30 m (V_{S30}) provide further insights into the geophysical characteristics of the study region. Bouguer gravity anomaly throughout the study region exhibits low and high values. Low Bouguer gravity anomalies are observed in the inland region, where granite is widely distributed (Jo & Hong, 2013) (Figure 2). High Bouguer gravity anomalies appear along the east coast where the Moho depth is relatively shallow (Lim et al., 2019; Shin & Ko, 2019).

Isostatic gravity anomalies are correlated with surface geology (Shin & Ko, 2019). The heat flow distribution also varies gradually across the study region. The mean surface heat flow in Korea is ∼60 mW/m^2, being close to the

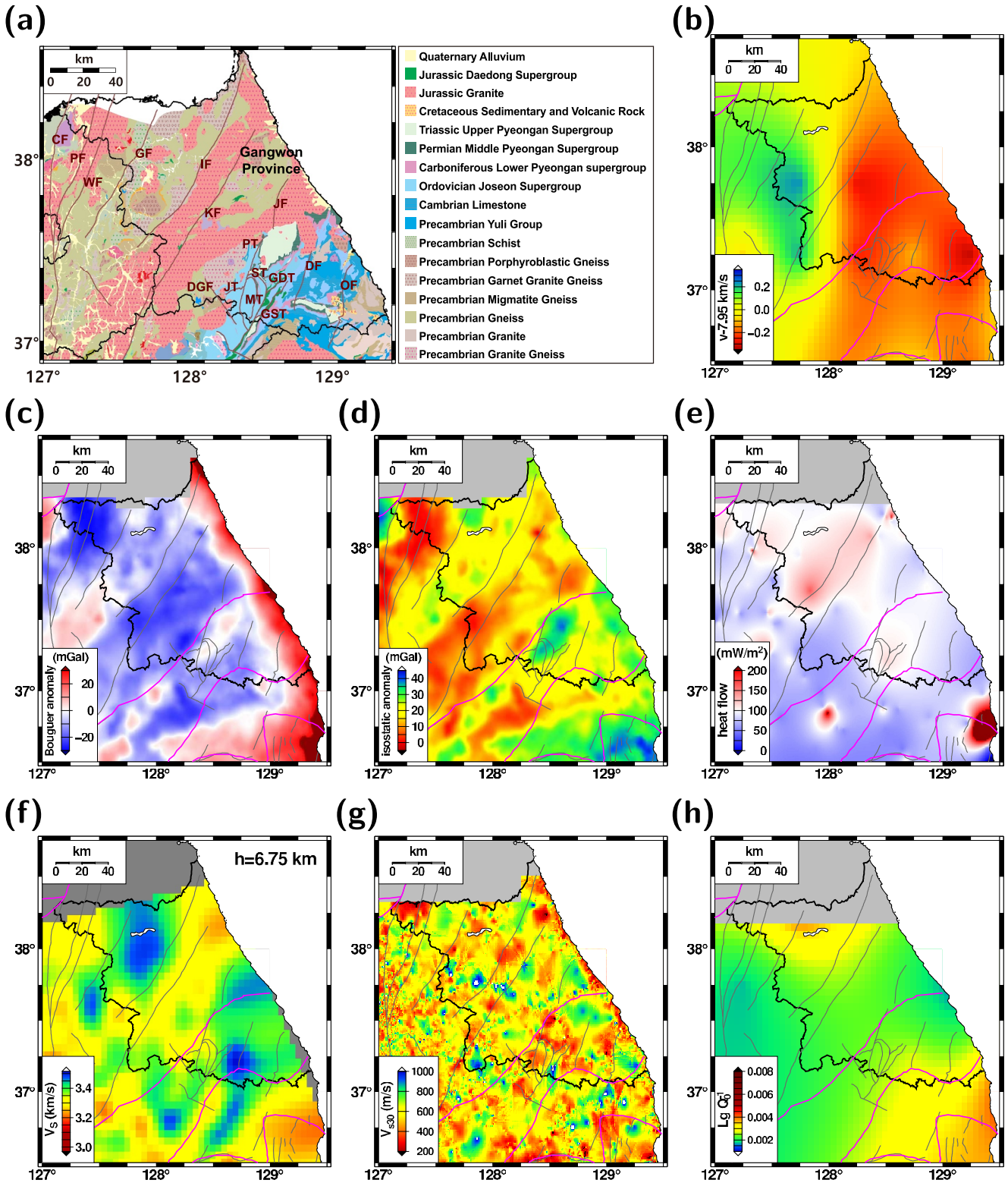

Figure 2.

global continental average (~65 mW/m^2) (Kim & Lee, 2007). The surface heat flow is relatively high in geologically young terranes (Kim & Lee, 2007). The southeastern and east-central Korean Peninsula present high heat flows of ≥~80 mW/m^2 (Kim & Lee, 2007). These thermal anomalies are related to past geodynamics including continental extension, mantle upwelling, and East Sea opening (Kim & Lee, 2007). The average shear-wave velocity at the top 30 m below the surface, V_{S30}, is linearly correlated with the topography. The V_{S30} is low along the coast, and relatively high in inland region (Kim & Hong, 2022). It is noteworthy that high gravity and magnetic anomalies are observed in Hupo bank, suggesting magmatic activity during the East Sea opening (Kim & Hong, 2022).

The central study region presents relatively low *Lg* attenuation (high quality factor, Q_0) compared to the southern and northern study regions (Hong, 2010). The Q_0 gradually decreases toward the east coast with significantly low values near the Hupo Bank and UB (Hong, 2010). These low Q_0 reflect the transition from continental to oceanic crusts in the East Sea and changes in medium properties due to continental rifting linked to the opening of the East Sea (Hong, 2010). Low and high mantle-lid *P* (*Pn*) velocities have been reported in the eastern-southern and western study regions, respectively (Hong & Kang, 2009). The *Pn* velocities appear to be correlated with the crustal structure (Hong & Kang, 2009). The *Pn* velocities in the eastern and coastal regions, as well as in the Okcheon fold belt region are low compared to the regions corresponding to Precambrian massifs. The presence of lower *Pn* velocities may reflect lithospheric deformation, such as continental collision, rifting, or uplift of the TBR (Choi et al., 2012; Hong & Kang, 2009).

3. Data

We analyze seismic records of 109 stations in the eastern Korean Peninsula. The seismic data are collected from the Korea Meteorological Administration (KMA; 70 broadband or short-period stations), Korea Institute of Geoscience and Mineral Resources (KIGAM; 11 broadband or short-period stations), and a temporal-deployed network (28 broadband stations) in the east-central Korean Peninsula (Figure 3). The sampling rates are 100 or 200 Hz. The interstation distances are 1.1–24.3 km, with an average of 11.7 km (Figure 3). The temporal seismic network has been in operation since June 2019.

We collect seismic records for 119 earthquakes with magnitudes $M_W \geq 6$ that occurred from January 2019 to January 2024 at distances ranging from 30° to 90° (Figure 3). The back azimuths of the events are predominantly distributed within the ranges of 30°–50°, 120°–225°, and 300°–315° (Figure 3). Seismic records with low quality, where precise *P*-wave arrivals could not be identified, are manually excluded from the analysis to ensure reliable phase picking and processing. The number of useful seismic events ranges from 19 to 104 at each station.

We collect the Rayleigh-wave group-velocity dispersion data for periods of 1–15 s from an ambient noise tomography study (Park & Hong, 2024) (Figure 4). We also collect the seismic waveforms for 13 regional shallow earthquakes in distances less than 10°. The focal depths are less than 40 km, and the magnitudes are ≥M_L4, to measure the long-period (5–60 s) group-velocity dispersions of Rayleigh and Love waves (Figure 4a).

4. Data Processing and Inversion Method

We calculate dispersion curves for fundamental-mode Rayleigh and Love waves in periods of 5–60 s from the seismic waveforms of 13 regional earthquakes using a multiple filter technique (Dziewonski et al., 1969; Herrmann, 1973). We combine the dispersion data from ambient noise tomography with those from regional event analyses. The dispersion curves from the two different data sets overlap at periods of ~15 s (Figure 4e).

To compute receiver functions, we apply a time-domain iterative deconvolution method that minimizes the misfit between the observed radial seismogram and a synthetic one, which is constructed by convolving a trial receiver function with the observed vertical P-wave signal (Kikuchi & Kanamori, 1982; Ligorría & Ammon, 1999). We

Figure 2. (a) Major geological structures and faults. The faults include Chugaryeong fault (CF), Pocheon fault (PF), Wangsukcheon fault (WF), Singal fault (SF), Gyeonggang fault (GF), Keumwang fault (KF), Inje fault (IF), Jinbu fault (JF), Osipcheon fault (OF), Dangok fault (DF), Danggol fault (DGF), Pyeongchang thrust (PT), Jucheon thrust (JT), Machari thrust (MT), Sangri thrust (ST), Gongsuwon thrust (GST) and Gakdong thrust (GDT) (Kim et al., 2002). Distribution of (b) mantle-lid *P*-wave (*Pn*) velocities (Hong & Kang, 2009), (c) Bouguer gravity anomalies (Lim et al., 2019), (d) Isotstatic anomalies (Lim et al., 2019), (e) heat flows on the surface (Kim et al., 2019), (f) shear-wave velocities at a depth of 6.75 km (Choi et al., 2009), (g) average shear-wave velocity at top 30 m below the surface (V_{S30}) (Kim & Hong, 2022), and (h) crustally-guided shear-wave attenuation factor ($Lg\ Q_0^{-1}$) (Hong, 2010).

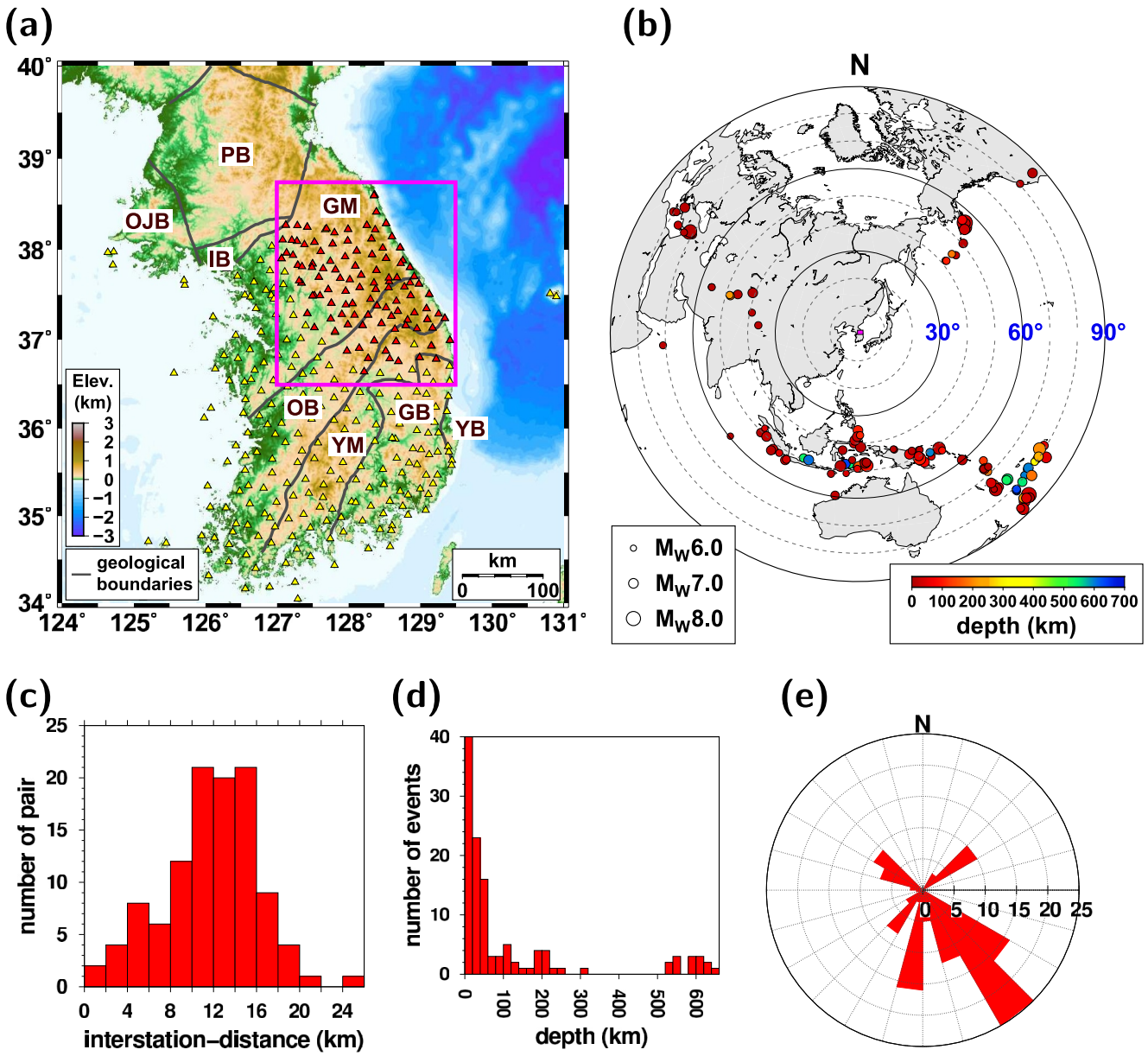

Figure 3. (a) Map of the Korean Peninsula and seismic stations. The study region is marked (boxed area). The geological provinces include Gyeonggi massif (GM), Imjingang belt (IB), Gyeongsang basin (GB), Okcheon belt (OB), Ongjin basin (OJB), Phyeong-nam basin (PB), Yeonil basin (YB), and Yeongnam massif (YM). Seismic stations (triangles) are presented. (b) Distribution of 93 teleseismic events analyzed for receiver function analysis. The event magnitudes and focal depths are marked. (c) Histogram of interstation distances in the study region. The interstation distances are less than 20 km in most regions. (d) Histogram of focal depths. Most focal depths are less than 150 km. (e) Azimuthal distribution of events for the stations. The events are distributed over wide azimuth ranges, being clustered in 120°–195°.

preprocess the three-component waveforms by removing the instrument response and applying a Butterworth bandpass filter with corner frequencies of 0.05 and 30 Hz. The waveforms are then rotated from the north-south, east-west, and vertical components to radial, tangential, and vertical components. We apply a Gaussian filter to the waveform window spanning from 10 s before to 50 s after the P-wave arrival (Figure 5). Two Gaussian width parameters (1.0 and 2.5) are tested to evaluate frequency sensitivity. Receiver functions with correlation less than 80% with theoretical receiver functions are excluded from further analysis. The selected high-quality receiver functions are then used in the stacking and joint inversion processes.

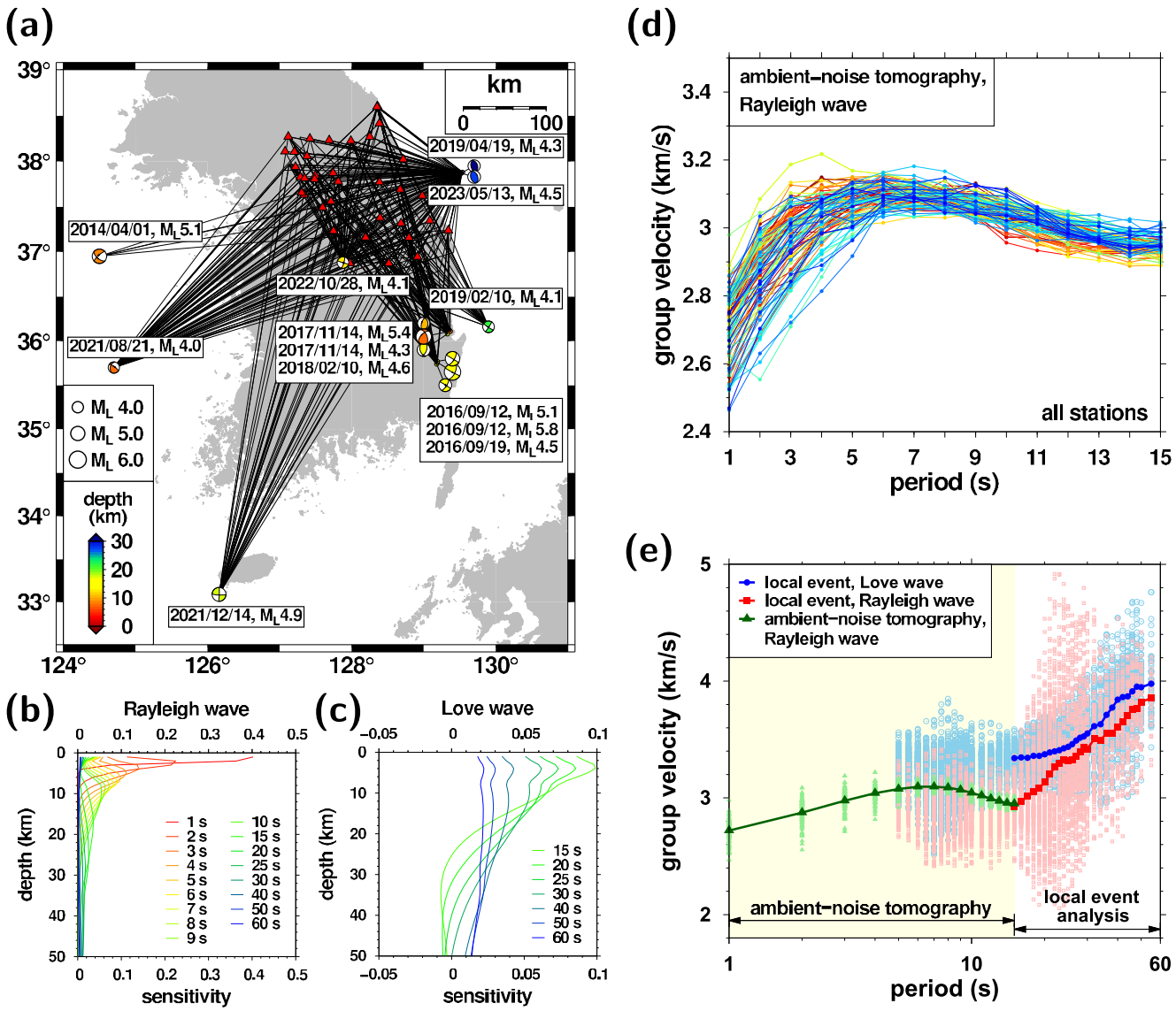

Figure 4. (a) Map of 13 local earthquakes analyzed for surface-wave dispersion analysis. The event information and focal mechanism solutions are presented. Raypaths to stations are marked (solid lines). Sensitivity kernels for (b) Rayleigh and (c) Love waves. (d) Group velocities of Rayleigh waves at stations in periods of 1–15 s from ambient noise tomography (Park & Hong, 2024). The group velocities vary mildly among the stations. (e) Combined surface-wave dispersion data. The group velocities of Rayleigh wave from ambient noise tomography (periods of 1–15 s) are combined with those from local earthquake analysis (periods of 5–60 s). The group velocities of Rayleigh waves at periods around 15 s are consistent between the two data sets.

We estimate the crustal thickness (Moho depth, H) and V_P/V_S ratio (κ) using an $H-\kappa$ stacking analysis (Zhu & Kanamori, 2000). This method involves stacking the amplitudes of three Moho-converted phases from the receiver functions (Zhu & Kanamori, 2000):

$$s(H,\kappa) = \omega_1 r(t_1) + \omega_2 r(t_2) + \omega_3 r(t_3), \quad (1)$$

where $r(t_i)$ is the receiver function amplitude at arrival time t_i, and ω_i ($i = 1, 2, 3$) are the weights for each phase ($\omega_1 = 0.7$, $\omega_2 = 0.2$, $\omega_3 = 0.1$). The arrival times t_1, t_2 and t_3 correspond to the *Ps*, *PpPs* and *PsPs* + *PpSs* phases, respectively. We search for the optimal values of H and κ that maximize $s(H,\kappa)$ (Figure 6). We search for the H between 18 and 40 km with a discrete interval of 0.1 km. We search for the optimum V_P/V_S ratios between 1.5 and 2.0 with an interval of 0.001. The Moho-converted phases observed in the data show good agreement with theoretical arrival times. We generate maps of Moho depth and V_P/V_S ratio by interpolating station-based

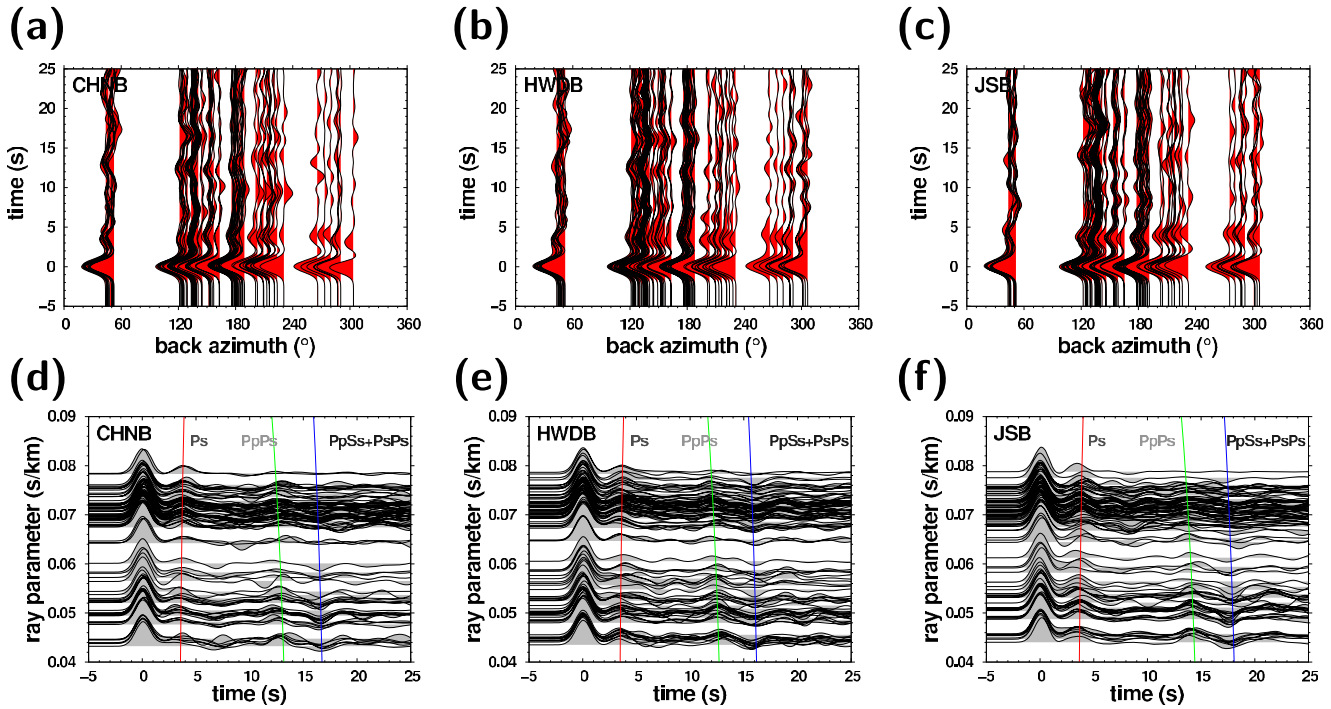

Figure 5. Examples of receiver functions with a Gaussian filter parameter (α) of 1.0 as a function of back azimuth at stations (a) CHNB, (b) HWDB, and (c) JSB. Receiver function profiles with a Gaussian filter parameter (α) of 1.0 as a function of the ray parameter at stations (d) CHNB, (e) HWDB, and (f) JSB. The theoretical arrival times of Moho-converted phases (*Ps*, *PpPs*, *PsPs* + *PpSs*) are indicated.

estimates using a kriging method over a grid with a spatial resolution of 0.005° in both latitude and longitude (Figure 7).

We apply an iterative least-squares inversion method to estimate the *S*-wave velocity model (Du & Foulger, 1999; Julià et al., 2000; Özalaybey et al., 1997). The optimal model minimizes the residuals between observed and synthetic receiver functions and surface-wave dispersion curves. The joint prediction error, E, is defined as

$$E = \frac{1-\gamma}{N_r}\sum_{i=0}^{N_r}\left[\frac{r(t_i)|_{obs} - r(t_i)|_{pre}}{\sigma_i}\right]^2 + \frac{\gamma}{N_s}\sum_{j=0}^{N_s}\left[\frac{d_j|_{obs} - d_j|_{pre}}{\sigma_j}\right]^2, \quad (2)$$

where $r(t_i)|_{obs}$ is the observed receiver function at time t_i, $r(t_i)|_{pre}$ is the predicted receiver function at time, t_i σ_i is the corresponding standard deviation of the receiver function data set, $d_j|_{obs}$ is the observed jth surface wave dispersion, $d_j|_{pre}$ is the predicted jth surface wave dispersion, σ_j is the standard deviation of the jth surface wave dispersion data set, N_r is the number of receiver function data, N_s is the number of surface wave dispersion data. The influence factor (γ) enables us to control the relative weighting between the receiver function and surface wave dispersion data, with a range of 0–1. Velocity models are inverted based only on the surface-wave dispersion analysis when $\gamma = 1$. On the other hand, the velocity models are entirely dependent on the receiver function analysis when $\gamma = 0$.

We apply the inversion with these parameters to real data at each station. We consider a half-space velocity model for the initial model with a layer thickness of 1 km. The density in the medium is determined by an empirical relationship with *P*-wave velocity (Berteussen, 1977). The inversion is conducted in two steps. We exclude the receiver functions with low correlation (less than 70%) with the theoretical receiver functions generated from the inverted model. A second-round inversion provides the final velocity model (Figure 8).

To determine optimal inversion parameters (γ, η), we conduct synthetic recovery tests using three reference models: (a) a layered model with linearly increasing velocity (m1), (b) a layered model with a low-velocity zone (m2), and (c) a gradually increasing velocity model representing the regional average (m3) (Figures 8e and 9a).

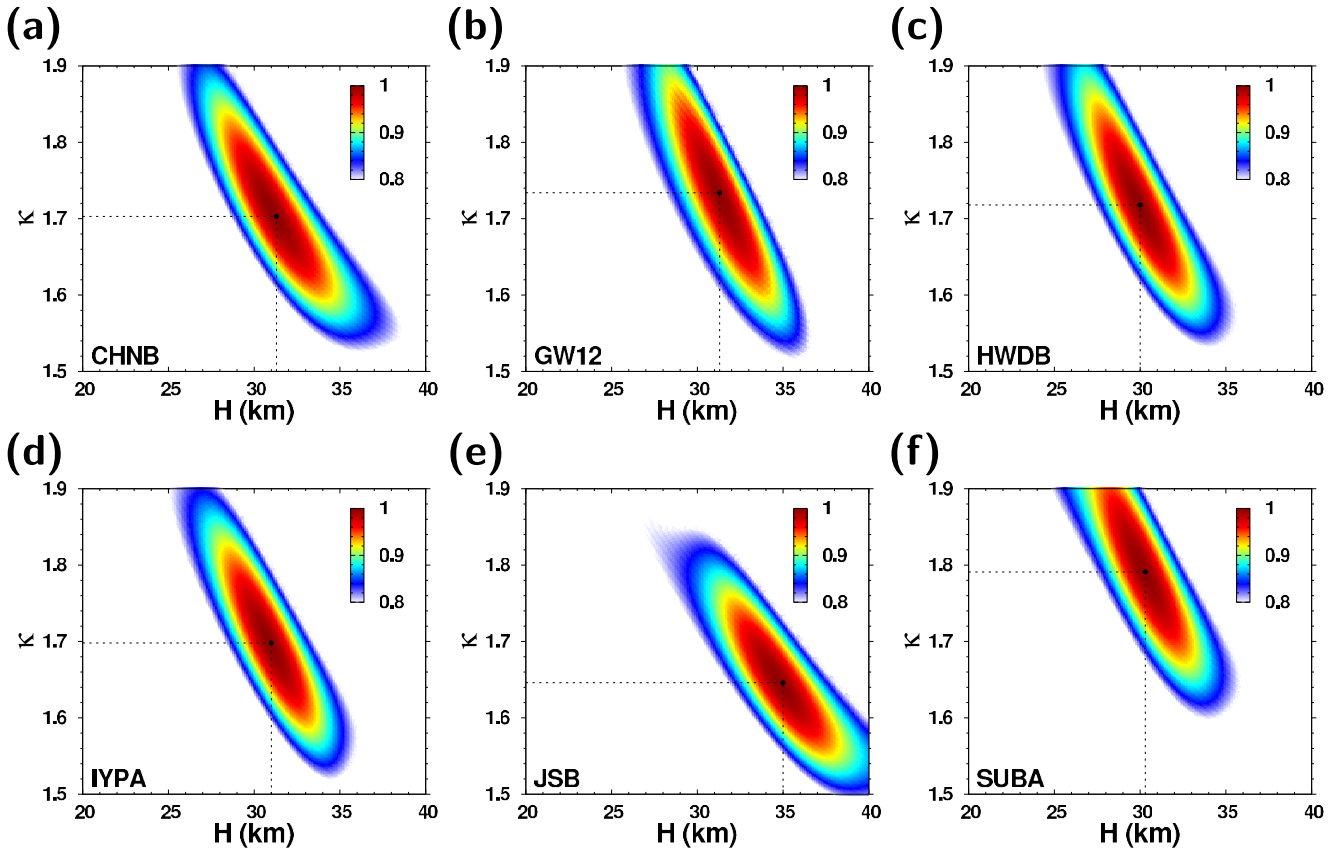

Figure 6. Example of crustal thickness (H) and V_P/V_S ratio (κ) analysis with a Gaussian filter parameter (α) of 1.0 at stations (a) CHNB, (b) GW12, (c) HWDB, (d) IYPA, (e) JSB, and (f) SUBA. The sets of crustal thicknesses and V_P/V_S ratios that maximize $s(H,\kappa)$ are marked.

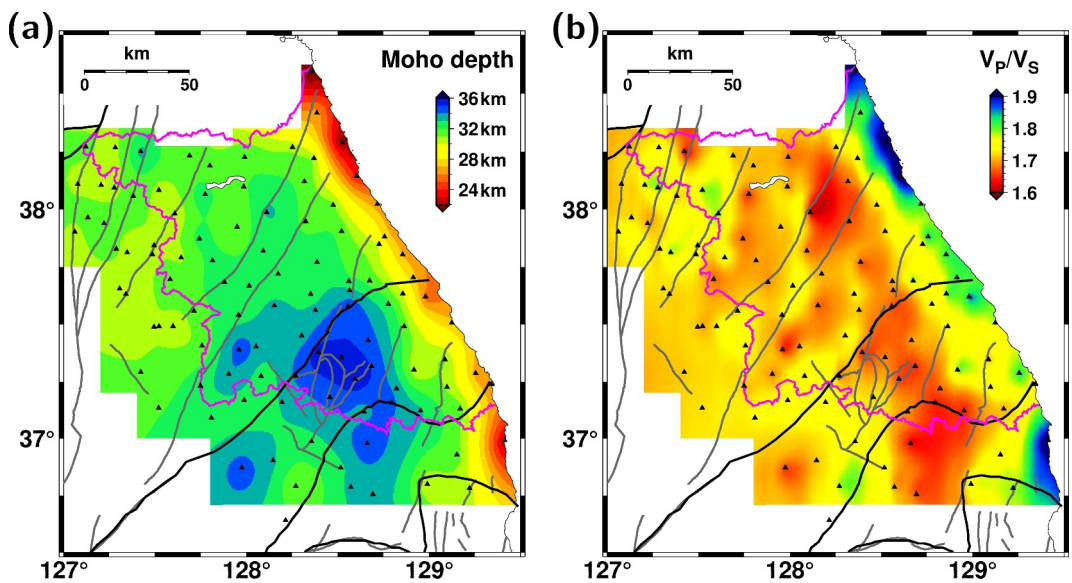

Figure 7. Lateral variations in (a) crustal thicknesses (Moho depths) and (b) V_P/V_S ratios determined by the $H-\kappa$ analysis. Fault traces and geological boundaries (solid lines) are marked. Stations (triangles) are indicated. High lateral variations in Moho depths and V_P/V_S ratios are observed.

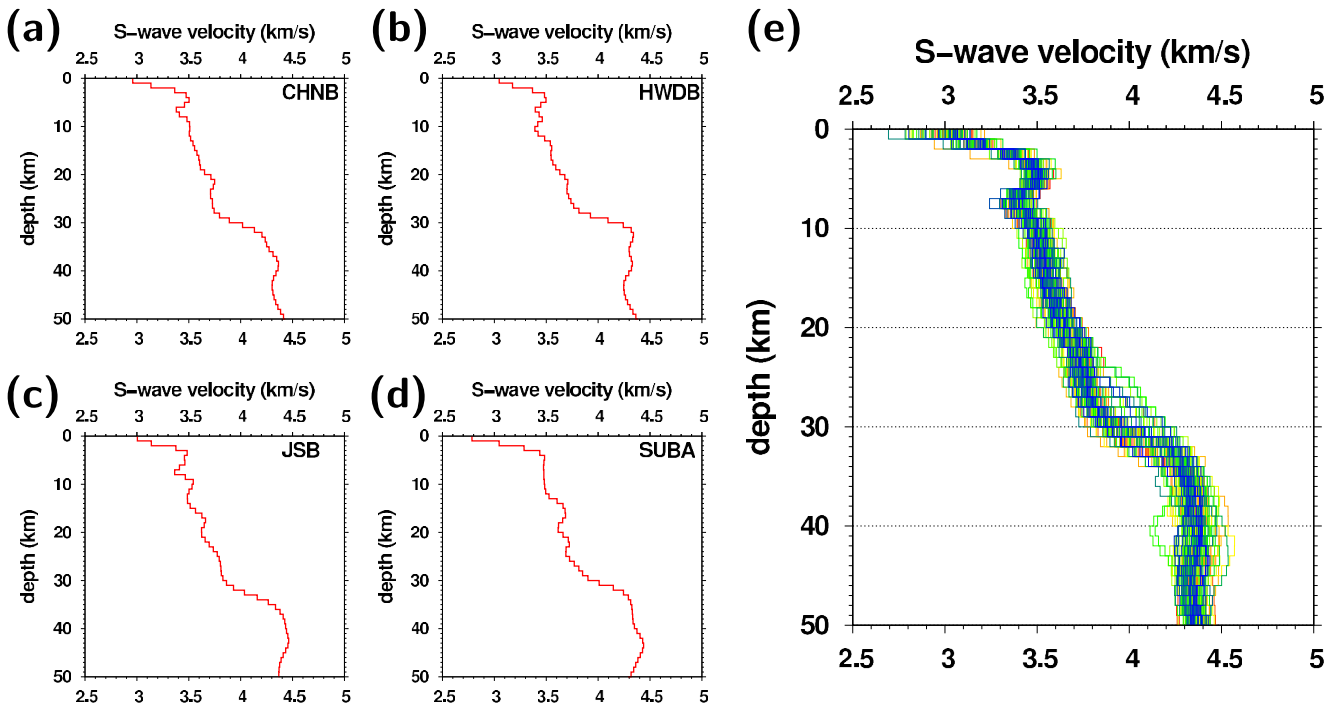

Figure 8. Inverted 1-D shear-wave velocity models at stations (a) CHNB, (b) HWDB, (c) JSB (d) SUBA, and (e) all stations. The shear-wave velocity models vary mildly among stations.

We calculate the synthetic receiver functions and surface wave dispersion data from the three models using the Thomson-Haskell matrix method (Herrmann, 2013). We conduct a joint inversion analysis for the synthetic receiver function and dispersion data with varying influence factor (γ) and damping factor (η) (Figure 9). The influence factor varies between 0 and 1. The damping factor changes between 0.1 and 0.9. We calculate the root mean squares error (RMSE) between the input and inverted models. We use a trade-off curve to find an optimal set of parameters.

The RMSE generally decreases with increasing model deviation (first derivative regularization, R_1) (Figures 9b–9d) and model roughness (second derivative regularization, R_2) (Figures 9c–9e). The observation suggests that a discretely-varying velocity model may yield better fit results. The analyses with a damping factor of $\eta = 0.5$ and influence coefficient of $\gamma = 0.15$ present an optimum balance between model smoothness and data misfit, yielding the best-fit agreement with the input models.

We apply a kriging interpolation to 1-D velocity models at a spatial resolution of 0.005° in both longitude and latitude. We also determine the average 1-D shear-wave velocity structure and differential shear-wave velocities for the 1-D velocity models. We present shear-wave velocity cross-sections along selected profiles that are oriented perpendicular to the coastline.

5. Moho Depth and V_P/V_S Ratio

The $H - \kappa$ analysis presents optimal V_P/V_S ratios and Moho depths beneath stations (Figure 6). The Moho depth varies by location, presenting significant lateral variation. The coastal regions present relatively shallow Moho depths (~26 km) (Figure 7a). On the other hand, the inland regions present the typical Moho depths of continental crust (~30–36 km). We also find a localized thick (>35 km) crust in the region surrounding the TB. The Moho depth increases with distance from the coast, reaching the typical continental crustal thickness of ~32 km at distances beyond 30 km from the coast. This trend is consistent with crustal deformation by a coast-parallel tectonic event in the East Sea (Figure 7).

The Moho depths are generally inversely proportional to V_P/V_S ratios (Figure 7). The V_P/V_S ratios are ~1.8–1.9 along the coast, whereas inland regions exhibit values of ~1.60–1.75. High V_P/V_S ratios (~1.8–1.9) are primarily

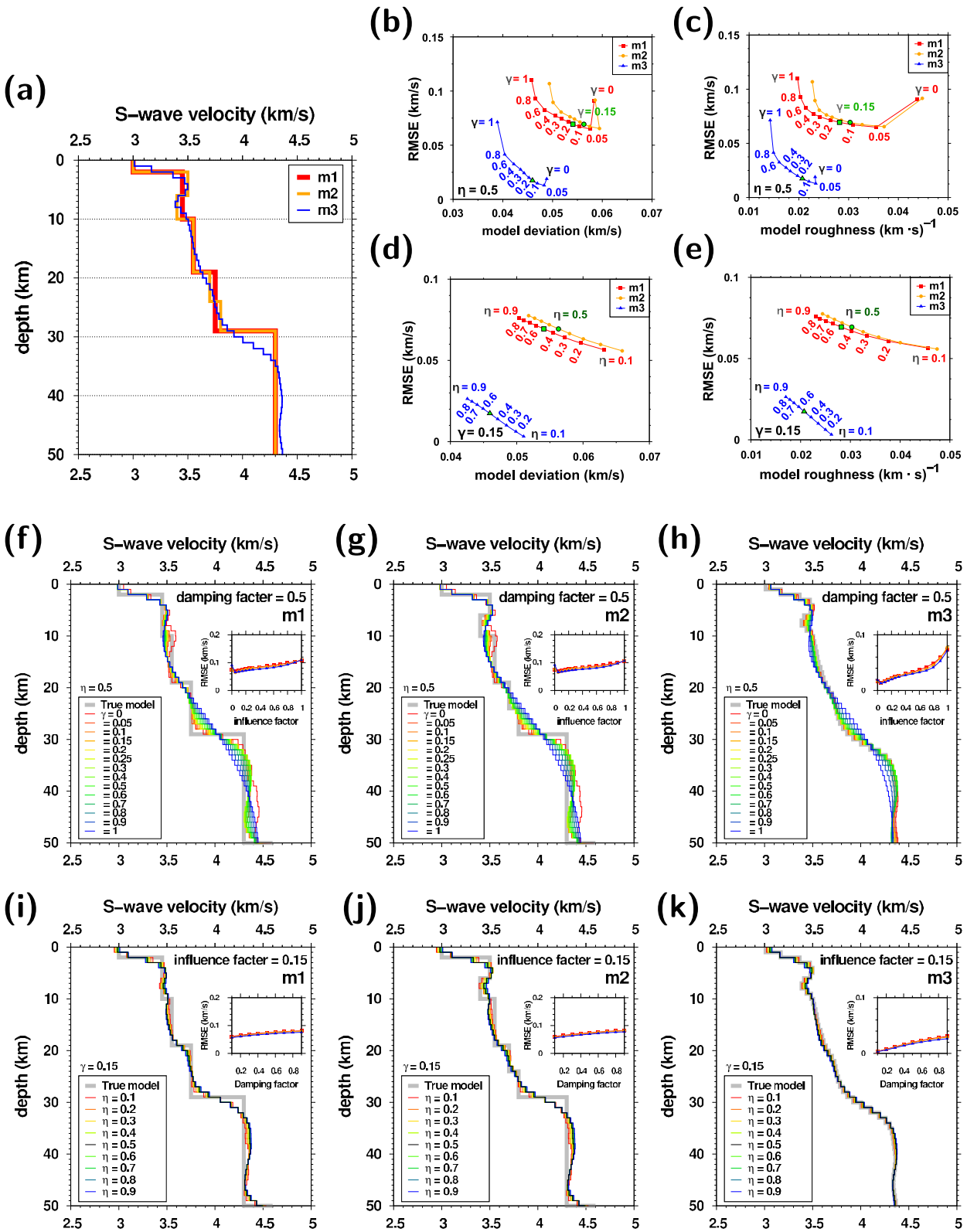

Figure 9.

observed along the coastal regions, whereas lower values (~1.60–1.75) are observed inland, particularly within the mountain range located 30–50 km from the coast. The observed high V_P/V_S ratios along the coast are likely associated with high pore fluid pressure and fracture anisotropy (Wang et al., 2012). On the other hand, high V_P/V_S ratios in the crust suggest mafic media that may be uplifted from the mantle (Christensen, 1996).

Also, inland regions show lower V_P/V_S ratios (~1.60–1.75), which are characteristic of continental crust. The northeastern part of study area around (38.25°N, 128.5°E) where volcanic activity was strong in the Eocene to the Miocene presents shallow Moho depths (~22 km) and high V_P/V_S ratios (~1.85) (Kil et al., 2007; Kim et al., 2012). The heat flow is high in the region (Kim et al., 2004).

We find a strong negative linear relationship between Bouguer gravity anomalies and crustal thicknesses (Moho depths) (Figure S10a in Supporting Information S1). We observe low Bouguer gravity anomalies in the regions of thick crust. Similarly, we find a mild negative correlation between heat flows and crustal thicknesses (Figure S10b in Supporting Information S1). The apparent correlations among seismic and geophysical properties suggest interlinked changes that may be dependent on tectonic evolution (Chen et al., 2021; He et al., 2014; Mandal et al., 2021; Murodov et al., 2018) (Figure 2c).

6. Shear-Wave Velocity Model

We determine 1-D shear-wave velocity models beneath stations (Figure 8). The 1-D structures change gradually among stations (Figure 8). We observe low-velocity layers at depths of ~14–22 km that vary by location (Figure 8). The Moho does not appear to be a sharp boundary. The shear-wave velocity increases gradually with depth around the Moho. The shear-wave velocity remains nearly constant beneath it, down to a depth of 50 km.

We interpolate the 1-D shear-wave velocity models to construct a 3-D shear-wave velocity model. Shear-wave velocities at shallow depths (≤3 km) present an apparent spatial correlation with geological features (Figure 2a). The Paleozoic sedimentary basin (TB) at latitudes of 37.0°–37.8° and longitudes of 128.0°–129.2° presents low shear-wave velocities. High shear-wave velocities appear in Proterozoic metamorphic regions and Mesozoic granitic regions. Also, the coastal areas present low shear-wave velocities at shallow depths (≤3 km), which is consistent with the V_{S30} distribution (Figure 2). These observations support apparent correlations between seismic velocities and geological structures.

Strong low velocities at shallow depths shallower than 3 km around the coast are likely associated with effective perturbed medium by a paleo tectonic event (Figure 10). Also, the shear-wave velocities are apparently high along the coast at depths of ~30 km (Figure 11). In particular, we observe distinct high-velocity anomalies with velocity difference of ≥0.2 km/s at depths of 26–32 km along the east coast in latitudes of 37°–38.5°. These high velocity anomalies indicate the uplifted media along the coast, suggesting that the continental rifting caused high medium deformation around the rift center.

The shear-wave velocities at depths of 10.5–14.5 km in the central Gyeonggi massif are lower than those in the surrounding regions by ~0.1 km/s (Figure 12). Also, there is a low velocity zone at depths of ~29 km in the area around the TB (Figure 12). This feature is consistent with the Moho depth variation. The low-velocity zone generally coincides with the low isostatic anomaly region where the heat flow is also low (≤100 mW/m^2) (Figure S10b in Supporting Information S1). We observe low heat flows in the eastern Gyeonggi massif around Keumwang fault (KF) and TB.

Shear-wave velocity contrasts appear at depths of 10–13 km along NE-SW trending faults. We find low-velocity anomalies between Gyeonggang fault and IF. On the other hand, high velocity anomalies appear between IF and KF. Also, we observe shear-wave velocity contrasts across the Jinbu fault at depths of 8–10 km and 13–15 km. These observations suggest that the fault zones act as structural boundaries, affecting the seismic velocities.

Figure 9. (a) Three input shear-wave velocity models (m1, m2, and m3). Trade off curves in inversion for damping factor of $\eta = 0.5$: (b) Root mean squares errors (RMSEs) as a function of model deviation (first derivative regularization, R_1), and (c) those as a function of model roughness (second derivative regularization, R_2). Trade off curves in inversion for a damping factor of $\gamma = 0.15$: (d) RMSEs as a function of model deviation, and (e) those as a function of model roughness. The optimal influence coefficient and the damping factor are indicated. Inversion with damping factor of $\eta = 0.5$ for input models (f) m1, (g) m2, and (h) m3, and with influence factor of $\gamma = 0.15$ for input models (i) m1, (j) m2, and (k) m3. The inverted models are compared. The RMSE of inverted velocity models to depths of 30 km (squares), 40 km (circles), and 50 km (triangles) are presented (inset).

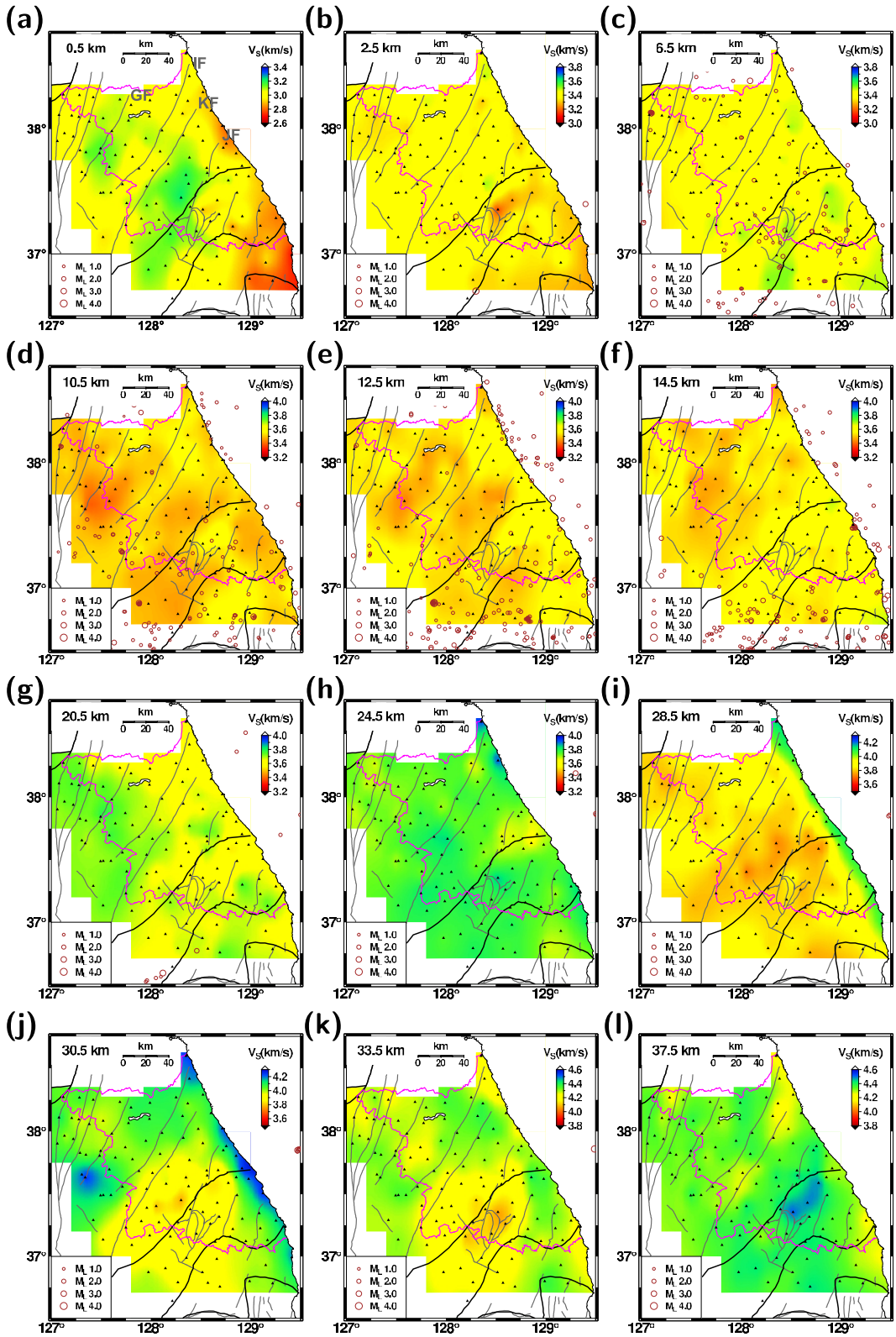

Figure 10. Shear-wave velocity models from joint inversion analysis with an influence factor of 0.15 at depths of (a) 0.5 km, (b) 2.5 km, (c) 6.5 km, (d) 10.5 km, (e) 12.5 km, (f) 14.5 km, (g) 20.5 km, (h) 24.5 km, (i) 28.5 km, (j) 30.5 km, (k) 33.5 km, and (l) 37.5 km. Fault traces and geological boundaries (solid lines) are presented. Earthquakes at the depths (circles) are marked. The shear-wave velocities change laterally.

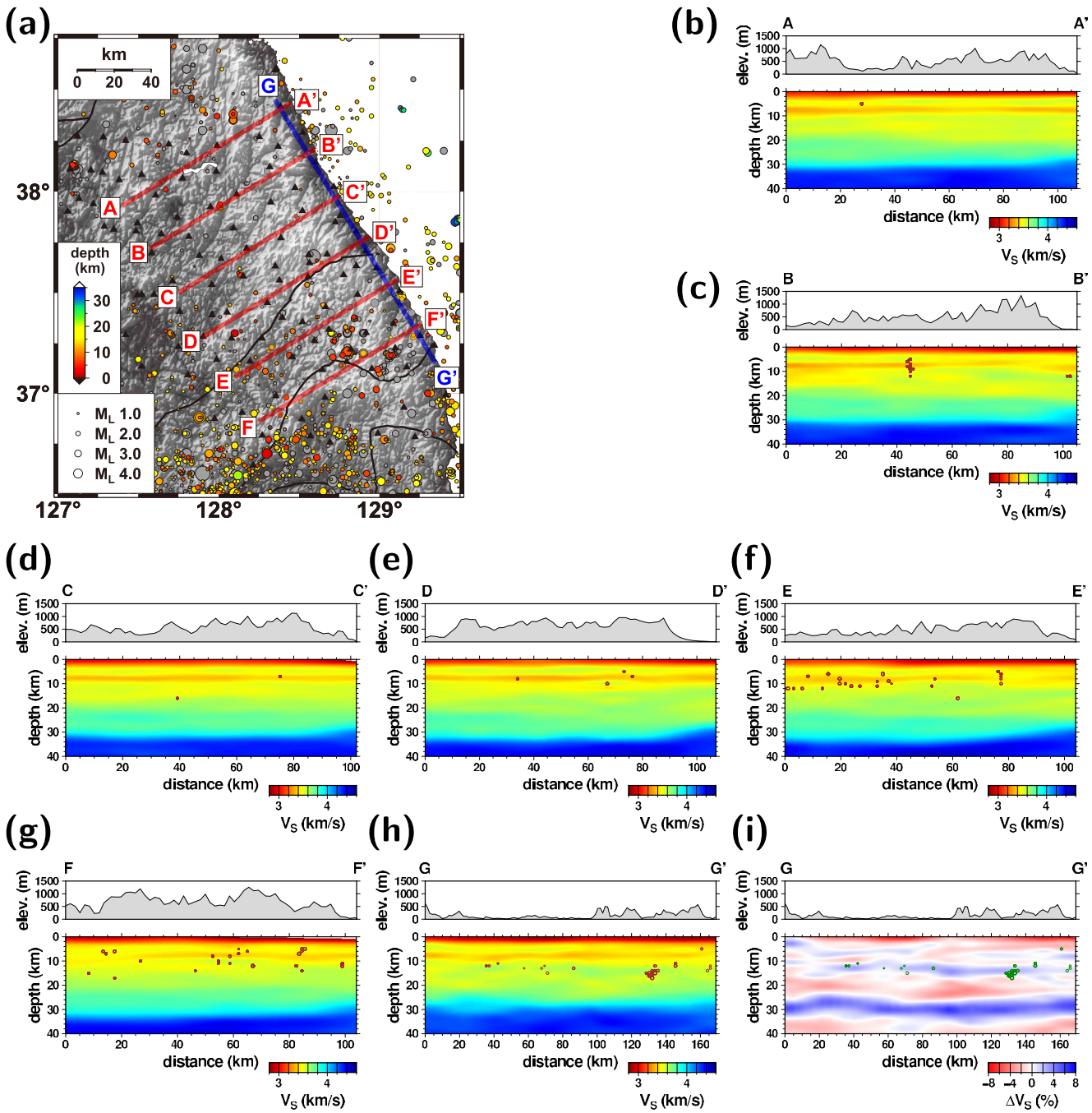

Figure 11. (a) Map of cross-section profiles with stations and seismicity. Shear-wave velocity structure along profiles (b) AA', (c) BB', (d) CC', (e) DD', (f) EE', (g) FF', and (h) GG'. (i) Differential shear-wave velocity model along profile GG'. High velocity anomalies appear at depths of ~30 km. The surface topography and seismicity along the profiles are presented on the shear-wave velocity models.

The seismicity is relatively high in the southern part of the study area, including the OB. Earthquakes mostly occur at depths of <12 km in inland regions. The earthquakes occur in the velocity-contrast locations with shear-wave velocities of ~3.6 km/s (Figure 12). The locations of lateral velocity contrasts may correspond to medium boundaries. On the other hand, earthquakes hardly occur in higher velocity regions. This feature suggests a correlation between seismicity and seismic velocities (Bem et al., 2020; Li et al., 2023; Lü et al., 2022). This observation suggests that the regions of velocity contrasts may indicate the potential locations of earthquakes.

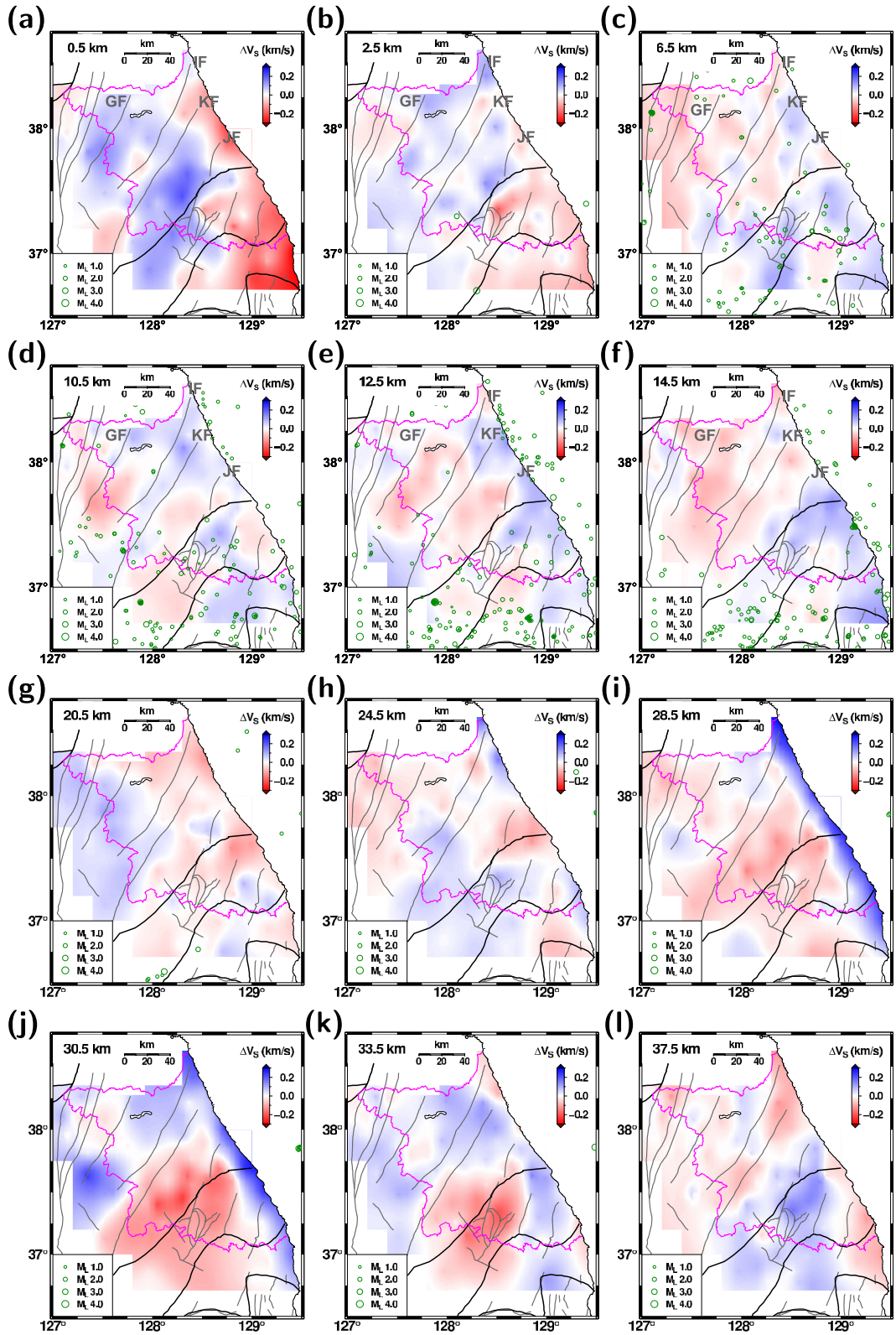

Figure 12. Differential shear-wave velocity models from joint inversion analysis with an influence factor of 0.15 at depths of (a) 0.5 km, (b) 2.5 km, (c) 6.5 km, (d) 10.5 km, (e) 12.5 km, (f) 14.5 km, (g) 20.5 km, (h) 24.5 km, (i) 28.5 km, (j) 30.5 km, (k) 33.5 km, and (l) 37.5 km. Fault traces and geological boundaries (solid lines) are presented. Earthquakes at the depths (circles) are marked. Strong high velocity anomalies are present at depths ~25–35 km along the coast.

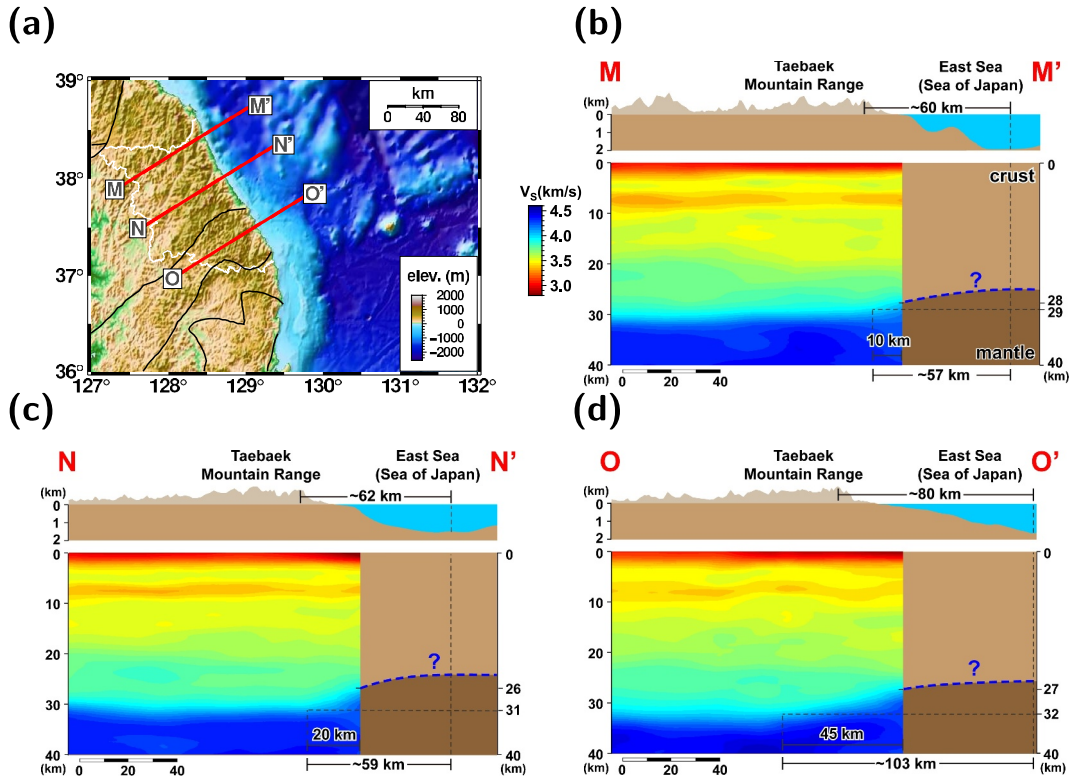

Figure 13. Schematic model of continent-side crust and upper mantle structure of the paleo rift in the East Sea (Sea of Japan): (a) map of three cross sections, and models for (b) cross section MM', (c) cross section NN' and (d) cross section OO'. Shear-wave velocity models are overlaid. Mantle is uplifted around the paleo rift. The mantle uplift appears beneath the coast. The uplift decreases with the distance from the paleo rifting center. The crustal thicknesses in offshore regions are extrapolated, being consistent with the CRUST1.0 model with 1°-by-1° resolution (dash lines) (Laske et al., 2013). The crustal thicknesses in the East Sea are presented using interpolation. The crustal thickness gradually decreases eastward to ~25 km.

Notably, the seismicity is high in the near offshore regions, where earthquakes are distributed along paleo-rift structures (Choi et al., 2012; Hong et al., 2024). Also, the maximum focal depths are laterally different. The focal depths in the offshore regions are 5–35 km (mostly in 15–20 km), while those in inland regions are 5–25 km (mostly in 5–10 km) (Figure S11 in Supporting Information S1). The focal depths in offshore regions are deeper due to the earthquake occurrence in the paleo-rift structures that extend across the crust.

The deep offshore seismogenic structures indicate preexisting paleo rift structures, which extend from the upper to the lower crust and Moho (Hong et al., 2020, 2024). The maximum focal depths of offshore events increase with distance from the coast, reaching depths of 15–30 km in the continental slope regions (Hong et al., 2024). This progression suggests a vertical extent of seismogenic structures within the paleo-rift zones. Further, the shear-wave velocities, Moho depth, and V_P/V_S ratios along the coast and high offshore seismicity indicate the presence of paleo rift structure near the coast. The continental rifting led to lateral variations in crustal thickness and crustal structures.

7. Rift Structure and Surface Morphology

The shear-wave velocity model provides information on the paleo-rift structures responsible for the East Sea opening. The shear-wave velocity anomalies suggest a coastline-parallel structure around the coast, which extends to the south. We examine the vertical structures along three profiles (MM', NN', and OO') across the coast (Figure 13). Here, the crustal thicknesses in offshore region are adopted from receiver function analysis with offshore stations and crustal model (CRUST1.0; Laske et al. (2013)) (see Supporting Information S1).

The inland peninsula displays continental crust properties with Moho depths of ~33 km. The typical Moho depth of continental crust in the inland peninsula decreases towards the coast. The Moho depths beneath the coast are

~24 km, which suggests a continental-to-oceanic transitional crust. The variations in Moho depth and V_P/V_S ratios between coastal and inland regions align with the features of continental rift.

Our findings align with previous studies that reported high-velocity anomalies at depths of 30–40 km along the east coast, associated with uplifted mantle (Park & Hong, 2024). The seismic velocity anomalies decrease with distance from the rift center. The development of the coastline-parallel UB, HB, Hupo fault (HF), and Hupo bank supports the geometry of the continental rift (Figure 14). Notably, low velocity anomalies appear at depths of 60–70 km beneath TBR and Korea Plateau (Song et al., 2020; Zheng et al., 2011). The low velocity anomalies indicate thermally elevated upper mantle (Kim et al., 2015; Song et al., 2020).

The crustal deformation in response to the continental rift appears to be extended inland, about >~30 km from the coast. The Moho uplift increases from 1 to 5 km to the south along the coast, expanding the uplifted area from ~10 to ~45 km from the coast (Figure 13). To estimate the strength of the uplift, we identify points of apparent change in slope of Moho surface from the cross-section. These points are used as reference locations to estimate the vertical uplift and width of the rifting process.

The TBR, developing along the coast presents an eastward-increasing (seaward-increasing) topography with the maximum elevation of 1.7 km. The mountain range with elevation of ≥300 m begin to appear at ~9–10 km from the coast westward (landward) on profiles MM', NN' and OO'. The peak elevations on the profiles are 1.0–1.2 km. On the other hand, the Moho surface starts to rise eastward (seaward) at ~10 km from the coast on profile MM', ~20 km from the coast on profile NN', and ~45 km from the coast on profile OO'.

The westward (landward) mountain range development and eastward (seaward) Moho uplift present a systematic variation to change in conjunction with relative position. We, thus, find three key features in the surface and Moho that include (a) a Moho uplift along the east coast, (b) surface uplift near the coast, most prominently in the TBR, and (c) distinct spatial offset between Moho and surface uplifts. The TBR exhibits characteristics similar to other rift flank uplifts, including the Rwenzori Mountains in the East African Rift System (Karner et al., 2000; Sachau et al., 2013), the Asir and Hejaz Mountains in the Red Sea Rift (Bohannon, 1986; Mukhopadhyay et al., 2024; van der Beek et al., 1994), the Sangre de Cristo and Sacramento Mountains in the Rio Grande Rift (Brown and Phillips, 1999), and the Transantarctic Mountains in the West Antarctic Rift System (van Wijk et al., 2008).

According to the Airy isostasy model for a laterally homogeneous crust, the locations of high surface elevations generally coincide with the regions of thick crust. However, when the constituent materials are laterally heterogeneous and the medium experiences a complex tectonic evolution, the surface topography may be less correlated with the crustal thickness. The surface topography in the TBR and coastal region presents a weak correlation with the crustal thickness. Also, we observe apparent spatial offsets between the Moho uplift and surface topography as ~60 km on profile MM' ~62 km on profile NN', and ~80 km on profile OO'.

These spatial gap may be associated with coupled deformation in crust and mantle. Composite effects including isostatic rebound, depth-dependent extension, and lithospheric flexure have been proposed to account for rift-flank uplift (Braun & Beaumont, 1989; Chèry et al., 1992; Karner et al., 2000; Ruppel, 1995; Sachau et al., 2013; Weissel & Karner, 1989). Such spatial offsets between Moho and surface topography are widely observed in rift flanks (Huismans & Beaumont, 2011; Silva et al., 2023).

Numerical modeling supports the Moho and surface uplifts in the rift flank across various rift systems (Bohannon, 1986; Braun & Beaumont, 1989; Weissel & Karner, 1989; Chèry et al., 1992; Brown and Phillips, 1999; Karner et al., 2000; van Wijk et al., 2008; Sachau & Koehn, 2010; Sachau et al., 2013). The Moho and surface uplifts are closely linked in space with offsets (Braun & Beaumont, 1989; Chèry et al., 1992; Ruppel, 1995). Also, the magnitude and extent of uplift depend on lithospheric strength (Chèry et al., 1992; Ruppel, 1995; Sachau et al., 2013). The numerical modeling consistently predicts surface uplifts of 1–5 km and Moho uplifts of 1–15 km depending on the rheology, lithospheric structure, and boundary conditions (Brown and Phillips, 1999; Chèry et al., 1992; Sachau et al., 2013; van Wijk et al., 2008; Weissel & Karner, 1989). The observed peak elevation of TBR (1.7 km) agrees with the numerical modelings. These suggest that flexural and isostatic mechanisms may explain the observed rift flank features.

It was suggested that the back-arc rifting initiated in the Japan Basin causing an E-W extension of the continental crust and leading to the HB formation (Figure 14) (Kim et al., 2022; Yoon & Chough, 1995). Subsequently, a crustal breakup occurred on the continental shelf, initiating seafloor spreading in the UB (Kim et al., 2022). A

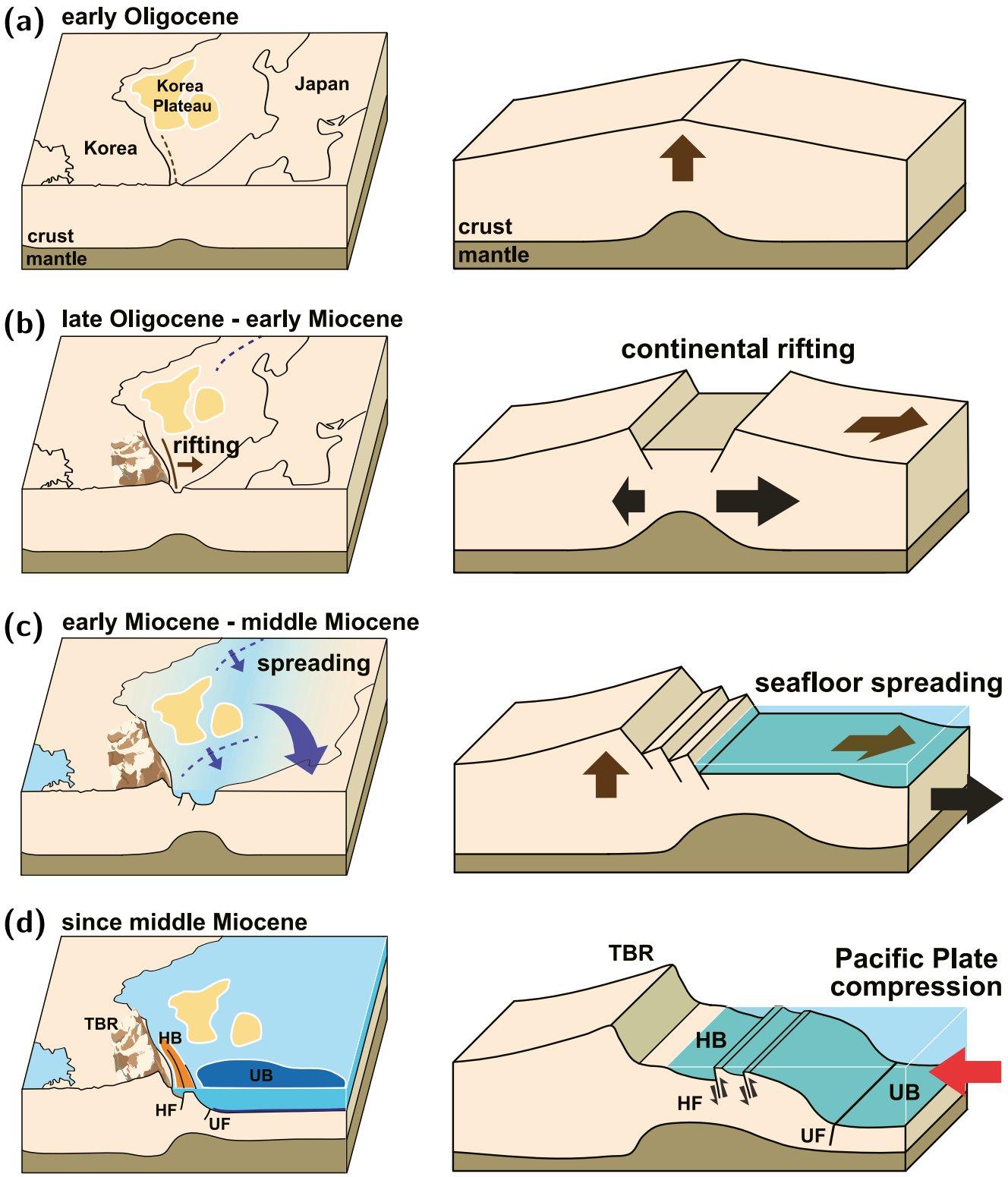

Figure 14.

continental rifting incorporates a series of evolutionary uplifts (Chèry et al., 1992; Sachau & Koehn, 2010). We observe considerable surface uplift in the east coast. Also, surface uplift (1–1.7 km) is much smaller than Moho uplift (1.5–4.9 km). These observations suggest that the TBR has likely not reached the post-rift equilibrium phase (Figure 14).

Numerous studies reported low-velocity anomalies at shallow depths along the east coast of the Korean Peninsula, supporting the presence of mantle upwelling (Kim et al., 2003, 2007, 2015; Park & Hong, 2024; Song et al., 2020). The mantle upwelling may facilitate continental breakup, inducing Moho uplift by thermal buoyancy (Chiarabba et al., 2020; Franke, 2013). Surface uplift occurs during lithospheric extension (lithosphere thinning) (McKenzie, 1978). The Moho and surface uplifts along rift flanks are additionally influenced by isostatic compensation, lithospheric necking, and flexural bending (Braun & Beaumont, 1989; Chèry et al., 1992; Karner et al., 2000; Sachau & Koehn, 2010; Weissel & Karner, 1989). The degree of surface uplift tends to increase with crustal rigidity (Braun & Beaumont, 1989; Chèry et al., 1992; Sachau et al., 2013). Thus, the surface deformation may be a result of composite effects of isostatic adjustment and flexural response as well as Moho uplift (Huismans & Beaumont, 2011; Lu & Huismans, 2021).

The numerical studies are consistent with the tectonic history of crustal stretching and thinning during the continental rift in the East Sea (Kim et al., 2003, 2007), followed by Moho uplift due to isostatic compensation (Braun & Beaumont, 1989; Weissel & Karner, 1989). The lateral variations in Moho depths, seismic velocity anomalies, surface morphology, and gravity anomalies suggest that the Moho uplift is subsequently followed by surface uplift, shaping the present-day topography eventually. These observations suggest that the TBR formed as a rift flank uplift, driven by extensional tectonics associated with the opening of the East Sea (Figure 14).

8. Discussion and Conclusions

The continental-side paleo-rift structure in the east-central Korean Peninsula is investigated using a joint inversion analysis based on receiver functions and surface-wave dispersions. Receiver function analysis precisely determines crustal thickness and V_P/V_S ratios. The joint inversion yields 1-D vertical structures beneath densely-deployed stations, allowing us to image laterally-varying crustal structures. We integrated the 1-D vertical structures at densely distributed stations to construct a 3-D shear-wave velocity model. The 3-D model provides high resolution in both lateral and vertical directions.

The shear-wave velocity model highlights features of tectonic evolution associated with continental rifting. The Moho depths in inland regions are ∼33 km corresponding to typical continental crust thickness. On the other hand, the Moho depths along the coast are considerably shallower (∼24 km), presenting a continental-to-oceanic transitional crust. Similarly, the V_P/V_S in inland regions are around 1.60–1.75, while those along the coast are around 1.8–1.9.

Shear-wave velocities present distinct vertical and lateral variations that are closely linked to geological and tectonic features. Inland areas are characterized by relatively low shear-wave velocities at shallow depths (≲3 km) around the TB that are covered by Paleozoic sedimentary rocks. The low-velocity anomalies at lower crust (∼29 km) beneath the TB agree with the presence of thick crust. Lateral velocity contrasts in the middle crust (∼10–15 km) are observed around major NE-SW trending faults such as the Gyeonggang, Inje, Keumwang, and Jinbu faults, suggesting that these structures serve as crustal boundaries influencing regional seismicity. On the other hand, coastal regions present laterally-varying deformed crustal structures that are related to paleo-rifting processes. Low-velocity anomalies are observed at shallow depths (≲3 km) along the east coast. Strong high-velocity anomalies are closely aligned with the coast at greater depths (∼30 km), suggesting localized mantle uplift associated with rifting processes.

Figure 14. Schematic tectonic evolution models for the East Sea opening and Taebaek Mountain Range (TBR) formation: (a) early Oligocene, (b) late Oligocene to early Miocene, (c) early to middle Miocene, and (d) since middle miocene. The left panel presents major tectonic episodes (Kim et al., 2015, 2018, 2022), while the right panel illustrates tectonic phases with associated forces and crustal deformation. The major structures are indicated (Kim et al., 2003; Lee & Kim, 2024): Ulleung Basin, Hupo Basin, Hupo fault, Ulleung fault, and TBR. In early Oligocene, continental rifting is initiated. In late Oligocene to early Miocene, continental rifting continues, causing Moho uplift and crustal extension. In early to middle Miocene, seafloor spreading commences following the continental breakup. Since middle Miocene, major structures in the East Sea are formed.

The shear-wave velocity model and Moho depth variation provide constraints on the dimensions of continental rift. The Moho uplift that is strong near the coast. We find that the continental-side rift structure appears to extend >30 km from the coast. This provides insights into the influence of continental rifting on the crustal structure including mountain range formation and Moho uplift. The low shear-wave velocities in shallow media (≤3 km) near the coast reflect crustal deformation associated with rifting. Also, the lateral variation in Moho depths and surface morphology indicate that the rift center may be located offshore near the coast. This feature is consistent with the geological evidence that the Hupo and Ulleung basins developed during East Sea opening (Figure 14). High gravity anomalies, low *Pn* velocities, high V_P/V_S ratios (1.8–1.9), and shallow Moho depths along the coast reflect crustal thinning toward the offshore rift center.

We observe the Moho uplift and mountain range development along the east coast that corresponds to the continent-side rift flank. Further, there are distinct spatial offsets between Moho and surface uplifts. Such features may be associated with mechanical response of lithosphere during continental rifting. The isostatic rebound for mass redistribution during continental rifting may lead to lithospheric uplift (Braun & Beaumont, 1989; Karner et al., 2000; Weissel & Karner, 1989). In particular, a depth-dependent stretching by mantle extension induces lithospheric uplift to maintain isostatic equilibrium, which may occur beneath a rift flank (Braun & Beaumont, 1989; Huismans & Beaumont, 2011; Karner et al., 2000; Lu & Huismans, 2021; Rowley & Sahagian, 1986; Royden & Keen, 1980; Weissel & Karner, 1989). Thus, these non-coaxial asymmetric uplifts of Moho and surface might result from the combined effect of depth-dependent stretching and isostatic adjustment.

A continental rift involves lithospheric thinning, incorporating crustal stretching, elevated heat flow, and magmatic underplating and intrusion (Ruppel, 1995). Thus, the observed features support the mantle-driven magmatism and mantle upwelling near the coast, suggesting the presence of nearby offshore rift center. The uplift pattern in the TBR presents characteristic rift flank features, which is commonly observed in extensional rift settings (Bohannon, 1986; Brown and Phillips, 1999; Karner et al., 2000; Mukhopadhyay et al., 2024; Sachau et al., 2013; van der Beek et al., 1994; van Wijk et al., 2008). Further, the observed surface and Moho uplifts agree with numerical modeling studies (Braun & Beaumont, 1989; Brown and Phillips, 1999; Chèry et al., 1992; Karner et al., 2000; Sachau et al., 2013; Sachau & Koehn, 2010; van Wijk et al., 2008; Weissel & Karner, 1989). We illuminated the vertical extent of crustal-scale structures from the receiver function analysis. We identified the Moho uplift and lithospheric thinning that developed in the course of continental rifting process.

These rifting-related processes such as mantle upwelling, Moho uplift, and surface deformation can be explained in broader geodynamic frameworks. The Big Mantle Wedge model suggests mantle upwelling induced by stagnant slab is a significant factor in the East Sea opening and Moho uplift (Zhao, 2021; Zhao et al., 2009). Slab rollback and extensional collapse models emphasize lithospheric extension and isostatic rebound (Itoh et al., 2006; Jolivet et al., 1994; Kim et al., 2003). These mechanisms collectively account for the structural features observed along the coast and the TBR.

The observed Moho uplift and elevated topography along the east coast of Korean Peninsula suggest local rift-flank structures for continental margin extension. Such rift flank uplifts are often observed in extensional tectonic regimes including Songliao Basin in Northeast China where elevated mountain ranges such as the Great Xing'an and Zhangguangcai Ranges are formed at the flank (Liu et al., 2001; Zhang et al., 2020; Zhou et al., 2023).

However, there are few coast-parallel surficial geological features in the inland region while the TBR develops along the coast. This observation suggests that the continental rifting might be effective in one side, separating the Japanese islands from the main land and holding the other side stationary (Figure 14). Such unilateral rifting might limitedly influence the crustal structures in the main land (Kim et al., 2007, 2015). Nevertheless, major offshore structures such as the HF extend coast-parallel, indicating potential rift-related deformation near the east coast. Further, the eastward-inclined surface topography of the TBR resembles the asymmetric uplift commonly observed along rift flanks.

We also find that earthquakes currently occur around velocity contrasts that may be associated with geological boundaries and paleo-tectonic structures (Choi et al., 2012; Hong et al., 2020, 2024; Kim et al., 2022; Shah et al., 2023). The observation suggests that the paleo-rift structures provide environments favorable for earthquake nucleation.

Data Availability Statement

The seismic waveforms are collected from the Korea Meteorological Administration (http://necis.kma.go.kr/) and Korea Institute of Geoscience and Mineral Resources (https://data.kigam.re.kr/quake/data/continuous-data). The data and results of this study are available on Dryad repository (Lee et al., 2025).

Acknowledgments
We thank Dr. Fenglin Niu (editor), anonymous associate editor, and two anonymous reviewers for constructive review comments. The seismic records were collected from Korea Meteorological Administration (KMA). This work was supported by the Korea Meteorological Administration Research and Development Program under Grant KMI2022-00710. Additionally, this research was partly supported by the Basic Science Research Program of National Research Foundation of Korea (RS-2017-NR023048).

References

Bae, H.-K., & Lee, H.-K. (2016). Quaternary activity patterns of the Wangsukcheon fault in the Pocheon-Namyangju area, Korea. *Journal of the Geological Society of Korea*, *52*(2), 129–147. (in Korean with English abstract). https://doi.org/10.14770/jgsk.2016.52.2.129

Bahat, D., & Paul, M. (1987). Horst faulting in continental rifts. *Tectonophysics*, *141*(1–3), 61–73. https://doi.org/10.1016/0040-1951(87)90174-0

Bem, T. S., Yao, H., Luo, S., Yang, Y., Wang, X., Wang, X., et al. (2020). High-resolution 3-D crustal shear-wave velocity model reveals structural and seismicity segmentation of the central-southern Tanlu Fault zone, eastern China. *Tectonophysics*, *778*, 228372. https://doi.org/10.1016/j.tecto.2020.228372

Berteussen, K. A. (1977). Moho depth determinations based on spectral-ratio analysis of NORSAR long-period P waves. *Physics of the Earth and Planetary Interiors*, *15*(1), 13–27. https://doi.org/10.1016/0031-9201(77)90006-1

Bohannon, R. G. (1986). Tectonic configuration of the western Arabian continental margin, southern Red Sea. *Tectonics*, *5*(4), 477–499. https://doi.org/10.1029/TC005i004p00477

Braun, J., & Beaumont, C. (1989). A physical explanation of the relation between flank uplifts and the breakup unconformity at rifted continental margins. *Geology*, *17*(8), 760–764. https://doi.org/10.1130/0091-7613(1989)017<0760:APEOTR>2.3.CO;2

Brown, C. D., & Phillips, R. J. (1999). Flexural rift flank uplift at the Rio Grande rift, New Mexico. *Tectonics*, *18*(6), 1275–1291. https://doi.org/10.1029/1999tc900031

Chang, S.-J., & Baag, C.-E. (2007). Moho depth and crustal Vp/Vs variation in southern Korea from teleseismic receiver functions: Implication for tectonic affinity between the Korean Peninsula and China. *Bulletin of the Seismological Society of America*, *97*(5), 1621–1631. https://doi.org/10.1785/0120050264

Chen, Y., Chen, J., Li, S., Yu, Z., Liu, X., & Shen, X. (2021). Variations of crustal thickness and average Vp/Vs ratio beneath the Shanxi Rift, North China, from receiver functions. *Earth Planets and Space*, *73*(1), 200. https://doi.org/10.1186/s40623-021-01528-8

Chèry, J., Lucazeau, F., Daignières, M., & Vilotte, J. P. (1992). Large uplift of rift flanks: A genetic link with lithospheric rigidity? *Earth and Planetary Science Letters*, *112*(1–4), 195–211. https://doi.org/10.1016/0012-821x(92)90016-o

Chiarabba, C., Bianchi, I., De Gori, P., & Agostinetti, N. P. (2020). Mantle upwelling beneath the Apennines identified by receiver function imaging. *Scientific Reports*, *10*(1), 19760. https://doi.org/10.1038/s41598-020-76515-2

Cho, M., Min, K., & Kim, H. (2018). Geology of the 2018 winter Olympic site, Pyeongchang, Korea. *International Geology Review*, *60*(3), 267–287. https://doi.org/10.1080/00206814.2017.1340196

Choi, D. K. (2014). *Geology and tectonic evolution of the Korean Peninsula*. Seoul National University Press. (in Korean with English summary).

Choi, H., Hong, T.-K., He, X., & Baag, C.-E. (2012). Seismic evidence for reverse activation of a paleo-rifting system in the East Sea (Sea of Japan). *Tectonophysics*, *572*, 123–133. https://doi.org/10.1016/j.tecto.2011.12.023

Choi, J., Kang, T.-S., & Baag, C.-E. (2009). Three-dimensional surface wave tomography for the upper crustal velocity structure of southern Korea using seismic noise correlations. *Geosciences Journal*, *13*(4), 423–432. https://doi.org/10.1007/s12303-009-0040-2

Chough, S. K., & Barg, E. (1987). Tectonic history of Ulleung basin margin, East Sea (Sea of Japan). *Geology*, *15*(1), 45–48. https://doi.org/10.1130/0091-7613(1987)15<45:THOUBM>2.0.CO;2

Christensen, N. I. (1996). Poisson's ratio and crustal seismology. *Journal of Geophysical Research*, *101*(B2), 3139–3156. https://doi.org/10.1029/95JB03446

Chung, D., Song, Y., Park, C., Kang, I.-M., Choi, S.-J., & Khulganakhuu, C. (2014). Reactivated timings of some major faults in the Chugaryeong fault zone since the Cretaceous period. *Economic and Environmental Geology*, *47*(1), 29–38. (in Korean with English abstract). https://doi.org/10.9719/eeg.2014.47.1.29

Cukur, D., Um, I.-K., Bahk, J.-J., Chun, J.-H., Horozal, S., Kim, S.-R., et al. (2018). Seismic stratigraphy and structural characteristics of the northeastern continental margin of Korea in the East Sea (Sea of Japan). *Marine and Petroleum Geology*, *98*, 706–717. https://doi.org/10.1016/j.marpetgeo.2018.09.013

Du, Z. J., & Foulger, G. R. (1999). The crustal structure beneath the northwest fjords, Iceland, from receiver functions and surface waves. *Geophysical Journal International*, *139*(2), 419–432. https://doi.org/10.1046/j.1365-246x.1999.00945.x

Dziewonski, A. M., Block, A., & Landisman, M. (1969). A technique for the analysis of transient seismic signals. *Bulletin of the Seismological Society of America*, *59*(1), 427–444. https://doi.org/10.1785/bssa0590010427

Franke, D. (2013). Rifting, lithosphere breakup and volcanism: Comparison of magma-poor and volcanic rifted margins. *Marine and Petroleum Geology*, *43*, 63–87. https://doi.org/10.1016/j.marpetgeo.2012.11.003

He, R., Shang, X., Yu, C., Zhang, H., & Van der Hilst, R. D. (2014). A unified map of Moho depth and Vp/Vs ratio of continental China by receiver function analysis. *Geophysical Journal International*, *199*(3), 1910–1918. https://doi.org/10.1093/gji/ggu365

Herrmann, R. B. (2013). Computer programs in seismology: An evolving tool for instruction and research. *Seismological Research Letters*, *84*(6), 1081–1088. https://doi.org/10.1785/0220110096

Herrmann, R. B. (1973). Some aspects of band-pass filtering of surface waves. *Bulletin of the Seismological Society of America*, *63*(2), 663–671. https://doi.org/10.1785/bssa0630020663

Hong, T.-K. (2010). Lg attenuation in a region with both continental and oceanic environments. *Bulletin of the Seismological Society of America*, *100*(2), 851–858. https://doi.org/10.1785/0120090057

Hong, T.-K., Baag, C.-E., Choi, H., & Sheen, D.-H. (2008). Regional seismic observations of the 9 October 2006 underground nuclear explosion in North Korea and the influence of crustal structure on regional phases. *Journal of Geophysical Research*, *113*(B3), B03305. https://doi.org/10.1029/2007JB004950

Hong, T.-K., Chung, D., Lee, J., Park, S., Kim, B., & Kim, W. (2021). Earthquake-spawning faults in the Seoul metropolitan area and their seismic implications. *Earth and Space Science*, *8*(7), e2021EA001662. https://doi.org/10.1029/2021EA001662

Hong, T.-K., & Kang, T.-S. (2009). Pn travel-time tomography of the paleo-continental-collision and rifting zone around Korea and Japan. *Bulletin of the Seismological Society of America*, *99*(1), 416–421. https://doi.org/10.1785/0120080120

Hong, T.-K., Park, S., & Houng, S. E. (2016). Seismotectonic properties and zonation of the far-eastern Eurasian plate around the Korean Peninsula. *Pure and Applied Geophysics*, *173*(4), 1175–1195. https://doi.org/10.1007/s00024-015-1170-2

Hong, T.-K., Park, S., Lee, J., & Kim, W. (2020). Spatiotemporal seismicity evolution and seismic hazard potentials in the western East Sea (Sea of Japan). *Pure and Applied Geophysics*, *177*(8), 3761–3774. https://doi.org/10.1007/s00024-020-02479-z

Hong, T.-K., Park, S., Lee, J., Lee, J., & Kim, B. (2024). Middle to lower crustal earthquakes in the western East Sea (Sea of Japan) and their implications for neotectonic evolution. *Tectonophysics*, *880*, 230346. https://doi.org/10.1016/j.tecto.2024.230346

Huismans, R., & Beaumont, C. (2011). Depth-dependent extension, two-stage breakup and cratonic underplating at rifted margins. *Nature*, *473*(7345), 74–78. https://doi.org/10.1038/nature09988

Itoh, Y., Uno, K., & Arato, H. (2006). Seismic evidence of divergent rifting and subsequent deformation in the southern Japan Sea, and a Cenozoic tectonic synthesis of the eastern Eurasian margin. *Journal of Asian Earth Sciences*, *27*(6), 933–942. https://doi.org/10.1016/j.jseaes.2005.09.008

Jo, E., & Hong, T.-K. (2013). Vp/Vs ratios in the upper crust of the southern Korean Peninsula and their correlations with seismic and geophysical properties. *Journal of Asian Earth Sciences*, *66*, 204–214. https://doi.org/10.1016/j.jseaes.2013.01.008

Jolivet, L., Tamaki, K., & Fournier, M. (1994). Japan Sea, opening history and mechanism: A synthesis. *Journal of Geophysical Research*, *99*(B11), 22237–22259. https://doi.org/10.1029/93JB03463

Julià, J., Ammon, C. J., Herrmann, R. B., & Correig, A. M. (2000). Joint inversion of receiver function and surface wave dispersion observations. *Geophysical Journal International*, *143*(1), 99–112. https://doi.org/10.1046/j.1365-246x.2000.00217.x

Karner, G. D., Byamungu, B. R., Ebinger, C. J., Kampunzu, A. B., Mukasa, R. K., Nyakaana, J., et al. (2000). Distribution of crustal extension and regional basin architecture of the Albertine rift system, East Africa. *Marine and Petroleum Geology*, *17*(10), 1131–1150. https://doi.org/10.1016/S0264-8172(00)00058-1

Khulganakhuu, C., Song, Y., Chung, D., Park, C., Choi, S.-J., Kang, I.-M., & Yi, K. (2015). Reactivated timings of Inje fault since the Mesozoic era. *Economic and Environmental Geology*, *48*(1), 41–49. (in Korean with English abstract). https://doi.org/10.9719/eeg.2015.48.1.41

Kikuchi, M., & Kanamori, H. (1982). Inversion of complex body waves. *Bulletin of the Seismological Society of America*, *72*(2), 491–506.

Kil, D., Hong, T.-K., Chung, D., Kim, B., Lee, J., & Park, S. (2021). Ambient noise tomography of upper crustal structures and Quaternary faults in the Seoul metropolitan area and its geological implications. *Earth and Space Science*, *8*(11), e2021EA001983. https://doi.org/10.1029/2021EA001983

Kil, Y.-W., Shin, H.-J., & Ko, B.-K. (2007). Magma pathway of alkali volcanic rocks in Goseong, Gangwon-do, Korea. *The Journal of the Petrological Society of Korea*, *16*(4), 196–207. (in Korean with English abstract).

Kim, B., & Hong, T.-K. (2022). A national Vs30 model for South Korea to combine nationwide dense borehole measurements with ambient seismic noise analysis. *Earth and Space Science*, *9*(1), e2021EA002066. https://doi.org/10.1029/2021EA002066

Kim, D.-E., Seong, Y. B., Byun, J., Weber, J., & Min, K. (2016). Geomorphic disequilibrium in the Eastern Korean Peninsula: Possible evidence for reactivation of a rift-flank margin. *Geomorphology*, *254*, 130–145. https://doi.org/10.1016/j.geomorph.2015.11.022

Kim, H.-J., Jou, H.-T., & Lee, G. H. (2018). Neotectonics of the eastern Korean margin inferred from back-arc rifting structure. *Ocean Science Journal*, *53*(3), 601–609. https://doi.org/10.1007/s12601-018-0036-9

Kim, H. C., Hwang, J.-H., & Baek, S.-G. (2019). *Geothermal flow distribution map*. Korea Institute of Geoscience and Mineral Resources. https://doi.org/10.22747/data.20201218.1518

Kim, H. C., Lee, S., & Song, M. Y. (2004). Geological characteristics and heat flow relationship in South Korea (Vol. *37*, pp. 391–400).

Kim, H. C., & Lee, Y. (2007). Heat flow in the Republic of Korea. *Journal of Geophysical Research*, *112*(B05413), B05413. https://doi.org/10.1029/2006JB004266

Kim, H.-J., Jou, H.-T., Cho, H.-M., Bijwaard, H., Sato, T., Hong, J.-K., et al. (2003). Crustal structure of the continental margin of Korea in the East sea (Japan sea) from deep seismic sounding data: Evidence for rifting affected by the hotter than normal mantle. *Tectonophysics*, *364*(1–2), 25–42. https://doi.org/10.1016/S0040-1951(03)00048-9

Kim, H.-J., Lee, G. H., Choi, D. L., Jou, H.-T., Li, Z., Zheng, Y., et al. (2015). Back-arc rifting in the Korea Plateau in the East sea (Japan sea) and the separation of the southwestern Japan Arc from the Korean margin. *Tectonophysics*, *638*, 147–157. https://doi.org/10.1016/j.tecto.2014.11.003

Kim, H.-J., Lee, G. H., Jou, H.-T., Cho, H.-M., Yoo, H.-S., Park, G.-T., & Kim, J.-S. (2007). Evolution of the eastern margin of Korea: Constraints on the opening of the East sea (Japan sea). *Tectonophysics*, *436*(1–4), 37–55. https://doi.org/10.1016/j.tecto.2007.02.014

Kim, H.-J., Moon, S., Kim, C., Kim, K. H., Seo, W., Cho, K. H., et al. (2022). Neotectonics at the SE continental margin of the Korean Peninsula: Implications for the back-arc region behind the SW Japan Arc. *Pure and Applied Geophysics*, *179*(11), 3945–3966. https://doi.org/10.1007/s00024-022-02979-0

Kim, H. S., Kil, Y., & Lee, M. W. (2012). The Formation of the cenozoic volcanic edifice in the goseong-ganseong area, gangwondo, Korea. *Journal of the Korean Earth Science Society*, *33*(7), 627–636. (in Korean with English abstract). https://doi.org/10.5467/JKESS.2012.33.7.627

Kim, J. C., Koh, H. J., Lee, S. R., Lee, C.-B., Choi, S.-J., Park, K.-H., et al. (2002). Digital geological map. *Korea Institute of Geoscience and Mineral Resources*. https://doi.org/10.22747/data.20231227.5375

Kim, K.-J., Yi, Yoo, D.-G., Yi, B.-Y., & Kang, N.-K. (2023). Seismic stratigraphy and structural evolution of the South Korea plateau, East Sea (sea of Japan). *Basin Research*, *36*(1), e12805. https://doi.org/10.1111/bre.12805

Kim, S. W., Oh, C. W., Williams, I. S., Rubatto, D., Ryu, I. C., Rajesh, V. J., et al. (2006). Phanerozoic high-pressure eclogite and intermediate-pressure granulite facies metamorphism in the Gyeonggi massif, South Korea: Implications for the eastward extension of the Dabie-Sulu continental collision zone. *Lithos*, *92*(3–4), 357–377. https://doi.org/10.1016/j.lithos.2006.03.050

Kwon, Y. K., Kwon, Y. J., Yeo, J. M., & Lee, C. Y. (2019). Basin evolution of the taebaeksan Basin during the early paleozoic. *Economic and Environmental Geology*, *52*(5), 427–448. (in Korean with English abstract).

Laske, G., Masters, G., Ma, Z., & Pasyanos, M. (2013). Update on CRUST1.0 A 1-degree global model of Earth's crust. *EGU General Assembly*.

Lee, J., Hong, T.-K., Lee, J., Park, S., & Kim, B. (2025). Continent-side paleo-rift structure in the western East Sea (Sea of Japan) and linkage between Moho uplift and mountain range formation [Dataset]. *Dryad*. https://doi.org/10.5061/dryad.ns1rn8q36

Lee, J.-H., & Kim, G.-B. (2024). The Hupo Basin, a neotectonic piggyback basin on the eastern Korean margin. *Geosciences Journal*, *28*(5), 671–685. https://doi.org/10.1007/s12303-024-0032-2

Li, J., Xu, J., Zhang, H., Yang, W., Tan, Y., Zhang, F., et al. (2023). High seismic velocity structures control moderate to strong induced earthquake behaviors by shale gas development. *Communications Earth and Environment*, *4*(1), 188. https://doi.org/10.1038/s43247-023-00854-x

Ligorría, J. P., & Ammon, C. J. (1999). Iterative deconvolution of teleseismic seismograms and receiver function estimation. *Bulletin of the Seismological Society of America*, *89*(5), 1395–1400. https://doi.org/10.1785/bssa0890051395

Lim, M., Shin, Y., Park, Y.-S., Rim, H., Ko, I. S., & Park, C. (2019). Digital gravity anomaly map of KIGAM. *Geophysics and Geophysical Exploration*, *22*(1), 37–43. (Korean with English abstract). https://doi.org/10.7582/GGE.2019.22.1.037

Liu, J., Han, J., & Fyfe, W. S. (2001). Cenozoic episodic volcanism and continental rifting in northeast China and possible link to Japan Sea development as revealed from K-Ar geochronology. *Tectonophysics*, *339*(3–4), 385–401. https://doi.org/10.1016/S0040-1951(01)00132-9

Lu, G., & Huismans, R. S. (2021). Melt volume at Atlantic volcanic rifted margins controlled by depth-dependent extension and mantle temperature. *Nature Communications*, *12*(1), 3894. https://doi.org/10.1038/s41467-021-23981-5

Lü, Z., Huang, H., Ye, X., Lü, J., & Xiong, C. (2022). High-resolution crustal shear-wave velocity structure in the pearl river delta, south China. *Seismological Research Letters*, *93*(1), 338–350. https://doi.org/10.1785/0220210116

Malehmir, A., Hong, T.-K., Lee, J., Zappala, S., Brodic, B., Chung, D., et al. (2022). Fault intersections control short period intraplate start-stop seismicity in the Korean Peninsula. *Tectonophysics*, *834*, 229387. https://doi.org/10.1016/j.tecto.2022.229387

Mandal, P., Srinivas, D., Suresh, G., & Srinagesh, D. (2021). Modelling of crustal composition and Moho depths and their Implications toward seismogenesis in the Kumaon-Garhwal Himalaya. *Scientific Reports*, *11*(1), 14067. https://doi.org/10.1038/s41598-021-93469-1

McKenzie, D. (1978). Some remarks on the development of sedimentary basins. *Earth and Planetary Science Letters*, *40*(1), 25–32. https://doi.org/10.1016/0012-821X(78)90071-7

Moon, S., Kim, H.-J., Kim, C., Lee, S.-H., Lee, S. H., & Kim, G.-B. (2023). Fault activity on the inner continental shelf of the SE Korean Peninsula associated with back-arc opening and closing in the NW Pacific subduction zone. *Marine Geophysical Researches*, *44*(1), 1. https://doi.org/10.1007/s11001-022-09510-z

Mukhopadhyay, M., Mukhopadhyay, B., Mogren, S., & Ibrahim, E. (2024). High velocity lower crust with anomalous rheological parameters under the Red Sea passive margin, SW Saudi arabia-insight into the evolution of the Hijaz-Asir escarpment zone. *Geophysical Journal International*, *236*(1), 711–726. https://doi.org/10.1093/gji/ggad451

Murodov, D., Zhao, J., Xu, Q., Liu, H., & Pei, S. (2018). Complex N-S variations in Moho depth and Vp/Vs ratio beneath the western Tibetan Plateau as revealed by receiver function analysis. *Geophysical Journal International*, *214*(2), 895–906. https://doi.org/10.1093/gji/ggy170

Otofuji, Y.-I. (1996). Large tectonic movement of the Japan Arc in late Cenozoic times inferred from paleomagnetism: Review and synthesis. *Island Arc*, *5*(3), 229–249. https://doi.org/10.1111/j.1440-1738.1996.tb00029.x

Özalaybey, S., Savage, M. K., Sheehan, A. F., Louie, J. N., & Brune, J. N. (1997). Shear-wave velocity structure in the northern Basin and Range province from the combined analysis of receiver functions and surface waves. *Bulletin of the Seismological Society of America*, *87*(1), 183–199. https://doi.org/10.1785/bssa0870010183

Park, C. H., Kim, J. W., Isezaki, N., Roman, D. R., & von Frese, R. R. (2006). Crustal analysis of the Ulleung Basin in the East Sea (Japan Sea) from enhanced gravity mapping. *Marine Geophysical Researches*, *27*(4), 253–266. https://doi.org/10.1007/s11001-006-9006-1

Park, S., & Hong, T.-K. (2024). Continent-side uplifted mantle and geological imprints along a paleo rift in the western East Sea (Sea of Japan). *Journal of Geophysical Research: Solid Earth*, *129*(9), e2024JB029049. https://doi.org/10.1029/2024JB029049

Park, S., Hong, T.-K., Kim, B., & Lee, J. (2023). Role of backbone fault system on earthquake spawning and geohazards in the Seoul metropolitan area. *Earth and Space Science*, *10*(3), e2022EA002686. https://doi.org/10.1029/2022EA002686

Park, S., Hong, T.-K., & Rah, G. (2021). Seismic hazard assessment for the Korean Peninsula. *Bulletin of the Seismological Society of America*, *111*(5), 2696–2719. https://doi.org/10.1785/0120200261

Park, S. J., & Son, I. (2005). Discussions on the distribution and genesis of mountain ranges in the Korean peninsular (I): The identification mountain ranges using a DEM and reconsideration of current issues on mountain range maps. *Journal of the Korean Geographical society*, *40*(1), 126–152. (in Korean with English abstract).

Rawlinson, N., Pozgay, S., & Fishwick, S. (2010). Seismic tomography: A window into deep earth. *Physics of the Earth and Planetary Interiors*, *178*(3–4), 101–135. https://doi.org/10.1016/j.pepi.2009.10.002

Rowley, D. B., & Sahagian, D. (1986). Depth-dependent stretching: A different approach. *Geology*, *14*(1), 32–33. https://doi.org/10.1130/0091-7613(1986)14<32:DSADA>2.0.CO;2

Royden, L., & Keen, C. E. (1980). Rifting process and thermal evolution of the continental margin of eastern Canada determined from subsidence curves. *Earth and Planetary Science Letters*, *51*(2), 343–361. https://doi.org/10.1016/0012-821X(80)90216-2

Ruppel, C. (1995). Extensional processes in continental lithosphere. *Journal of Geophysical Research*, *100*(B12), 24187–24215. https://doi.org/10.1029/95JB02955

Sachau, T., & Koehn, D. (2010). Faulting of the lithosphere during extension and related rift-flank uplift: A numerical study. *International Journal of Earth Sciences*, *99*(7), 1619–1632. https://doi.org/10.1007/s00531-010-0513-6

Sachau, T., Koehn, D., & Passchier, C. (2013). Mountain-building under extension. *American Journal of Science*, *313*(4), 326–344. https://doi.org/10.2475/04.2013.03

Sato, T., Sato, T., Shinohara, M., Hino, R., Nishino, M., & Kanazawa, T. (2006). P-wave velocity structure of the margin of the southeastern Tsushima Basin in the Japan Sea using ocean bottom seismometers and airguns. *Tectonophysics*, *412*(3–4), 159–171. https://doi.org/10.1016/j.tecto.2005.09.001

Shah, A. K., Pratt, T. L., & Horton Jr, J. W. (2023). Rift basins and intraplate earthquakes: New high-resolution aeromagnetic data provide insights into buried structures of the Charleston, South Carolina seismic zone. *Geochemistry, Geophysics, Geosystems*, *24*(5), e2022GC01080. https://doi.org/10.1029/2022GC010803

Shin, J., & Hwang, S. (2014). A critical review on setting up the concept, timing and mechanism of tertiary tilted flexural mode of the Korean peninsula: A new hypothesis derived from plate tectonics. *Journal of the Korean Geographical Society*, *49*(2), 200–220. (in Korean with English abstract).

Shin, J., & Sandiford, M. (2012). Neogene uplift in the Korean peninsula linked to small-scaled mantle convection at Sinking slab Edge. *Journal of the Korean Geographical Society*, *47*(3), 328–346.

Shin, Y. H., & Ko, I. S. (2019). Gravity anomaly in the Taebaeksan mineralized zone. *Journal of the Geological Society of Korea*, *55*(4), 403–413. (in Korean with English abstract). https://doi.org/10.14770/jgsk.2019.55.4.403

Silva, J. P. M., Sacek, V., & da Silva, R. M. (2023). The influence of lithospheric rheology and surface processes on the preservation of escarpments at rifted margin. *Tectonophysics*, *851*, 229769. https://doi.org/10.1016/j.tecto.2023.229769

Song, J.-H., Kim, S., & Rhie, J. (2020). Heterogeneous modification and reactivation of a craton margin beneath the Korean Peninsula from teleseismic travel time tomography. *Gondwana Research*, *81*, 475–489. https://doi.org/10.1016/j.gr.2019.11.016

Tamaki, K. (1988). Geological structure of the Japan Sea and its tectonic implications. *Chishitsu Chosasho Geppo*, *39*(5), 296–365.

van der Beek, P., Cloetingh, S., & Andriessen, P. (1994). Mechanisms of extensional basin formation and vertical motions at rift flanks: Constraints from tectonic modelling and fission-track thermochronology. *Earth and Planetary Science Letters*, *121*(3–4), 417–433. https://doi.org/10.1016/0012-821X(94)90081-7

van Wijk, J. W., Lawrence, J. F., & Driscoll, N. W. (2008). Formation of the Transantarctic mountains related to extension of the West Antarctic Rift System. *Tectonophysics*, *458*(1–4), 117–126. https://doi.org/10.1016/j.tecto.2008.03.009

Wang, X.-Q., Schubnel, A., Fortin, J., David, E. C., Guéguen, Y., & Ge, H.-K. (2012). High Vp/Vs ratio: Saturated cracks or anisotropy effects? *Geophysical Research Letters*, *39*(11), L11307. https://doi.org/10.1029/2012GL051742

Weissel, J. K., & Karner, G. D. (1989). Flexural uplift of rift flanks due to mechanical unloading of the lithosphere during extension. *Journal of Geophysical Research*, *94*(B10), 13919–13950. https://doi.org/10.1029/jb094ib10p13919

Yoon, S. H., & Chough, S. K. (1995). Regional strike slip in the eastern continental margin of Korea and its tectonic implications for the evolution of Ulleung Basin, East Sea (Sea of Japan). *Geological Society of America Bulletin*, *107*(1), 83–97. https://doi.org/10.1130/0016-7606(1995)107<0083:RSSITE>2.3.CO;2

Yu, S. H. (2006). *Development of gravity model and Moho discontinuity in the Korean Peninsula and its surrounding seas using GRACE geopotential data*. Ph.D. thesis. Yonsei University (in Korean).102.

Zappala, S., Malehmir, A., Hong, T.-K., Juhlin, C., Lee, J., Papadopoulou, M., et al. (2022). Crustal-scale fault systems in the Korean Peninsula unraveled by reflection seismic data. *Earth and Space Science*, *9*, e2022EA002464. https://doi.org/10.1029/2022EA002464

Zhang, C., Quan, J.-Y., Zhang, Y.-J., Liu, Z.-H., Li, W., Wang, Y., et al. (2020). Late Mesozoic tectonic evolution of the southern Great xing'an range, NE China: Evidence from whole-rock geochemistry, and zircon UPb ages and Hf isotopes from volcanic rocks. *Lithos*, *362*, 105409. https://doi.org/10.1016/j.lithos.2020.105409

Zhao, D. (2021). Seismic imaging of northwest pacific and East Asia: New insight into volcanism, seismogenesis and geodynamics. *Earth-Science Reviews*, *214*, 103507. https://doi.org/10.1016/j.earscirev.2021.103507

Zhao, D., Tian, Y., Lei, J., Liu, L., & Zheng, S. (2009). Seismic image and origin of the Changbai intraplate volcano in East Asia: Role of big mantle wedge above the stagnant Pacific slab. *Physics of the Earth and Planetary Interiors*, *173*(3–4), 197–206. https://doi.org/10.1016/j.pepi.2008.11.009

Zheng, Y., Shen, W., Zhou, L., Yang, Y., Xie, Z., & Ritzwoller, M. H. (2011). Crust and uppermost mantle beneath the North China Craton, northeastern China, and the Sea of Japan from ambient noise tomography. *Journal of Geophysical Research*, *116*(B12), B12312. https://doi.org/10.1029/2011JB008637

Zhou, J., Dunkl, I., Liu, Y., Li, S., Li, W., & von Eynatten, H. (2023). Cretaceous source to sink system reconstruction of northeastern Asian continental margin: Insight from integrated detrital geochronology in NE China. *Geoscience Frontiers*, *14*(5), 101616. https://doi.org/10.1016/j.gsf.2023.101616

Zhu, L., & Kanamori, H. (2000). Moho depth variation in southern California from teleseismic receiver functions. *Journal of Geophysical Research*, *105*(B2), 2969–2980. https://doi.org/10.1029/1999jb900322